High-frequency voltage-driven vibrations in dielectric elastomer membranes

Article *in* Mechanical Systems and Signal Processing · December 2021

DOI: 10.1016/j.ymssp.2021.108677

CITATIONS
5

READS
185

4 authors, including:

Giacomo Moretti
Universität des Saarlandes
62 PUBLICATIONS **639** CITATIONS
SEE PROFILE

Gianluca Rizzello
Universität des Saarlandes
159 PUBLICATIONS **1,367** CITATIONS
SEE PROFILE

Marco Fontana
Scuola Superiore Sant'Anna
129 PUBLICATIONS **1,915** CITATIONS
SEE PROFILE

High-frequency voltage-driven vibrations in dielectric elastomer membranes

Giacomo Moretti*[1], Gianluca Rizzello[1], Marco Fontana[2], and Stefan Seelecke[1]

[1]Intelligent Material Systems Laboratory, Saarland University, Saarbrücken, Germany
[2]Institute of Mechanical Intelligence, Scuola Superiore Sant'Anna, Pisa, Italy

Abstract

This article deals with modelling and experimental characterisation of the continuum dynamic response of dielectric elastomer actuators (DEAs) subject to high-frequency voltage excitation.
DEAs are capable of large deformations in response to an electrostatic stimulus, and they show large operating bandwidths of up to a few kilohertz. Although DEA systems normally make use of simple deformation patterns and a well-defined main actuation mode, they show complex structural dynamics and mode shapes if subject to high frequency voltage inputs. Taking advantage of these complex structural dynamics potentially allows developing multi-function actuators, audio devices and vibration isolators capable to perform different tasks using different vibration regimes.

We first present a multi-domain model for the structural dynamics of DEAs, accounting for the contribution of the air pressure loads generated the DEA membrane vibrations, which play a relevant role in the DEA dynamics.
We then present an extensive experimental characterisation of DEA samples' structural dynamics based on laser Doppler vibrometer measurements. In particular, we measure the complex structural mode shapes and the velocity spectra generated through a broadband excitation in correspondence of a wide set of different design and control parameters (namely, the DEA geometric layout, the mechanical-preload and the applied voltage bias).
Based on the experimental results, we validate the proposed continuum model, and we demonstrate that the forced response of the DEA can be efficiently described using a lumped-parameter computationally efficient reduced reformulation.

Keywords: dielectric elastomer; vibrations; natural frequencies; modelling; vibrometer; modal analysis; dynamics; acoustic-structure-interaction.

1 Introduction

Dielectric elastomer actuators (DEAs) are electrostatic transducers that exploit voltage-driven deformations of a stretchable polymeric dielectric membrane covered by compliant electrodes [1]. DEAs are capable of providing large actuation energy densities (on the order of 0.1-1 J/g per actuation cycle [2]),

*Corresponding author.
E-mail: giacomo.moretti@imsl.uni-saarland.de

present large operating bandwidths (up to the kHz range [3, 4]), and are made of lightweight and resilient materials. For these reasons, they offer promising perspectives for a wide range of applications, such as soft robots [5], fluidic systems [6], haptic interfaces [7], tunable lenses [8], or active vibration suppression devices [9].

Most of the current applications of dielectric elastomer (DE) systems exploit a single actuation mode, such that the DE membrane follows a predefined deformation pattern over the DEA's working frequency range. Such an actuation mode, also referred to as pumping mode, corresponds to the response that a DEA exhibits when a low frequency voltage input is applied. The pumping mode is largely exploited in static or low frequency dynamic applications, including resonant actuators [6] or energy harvesters [10]. In principle, complex deformation patterns can also be achieved, by taking advantage of the DE membranes structural dynamics, in the presence of high frequency or broadband voltage excitations [11]. The exploitation of such higher order mode shapes and deformations patterns opens up possibilities towards new designs and applications, such as multi-mode loudspeakers exploiting different deformation modes over different frequency ranges, or fluid dispensers that change their distribution patterns at different frequencies.

To date, only a few works have investigated the complex structural dynamics that take place in DEAs subject to high frequency excitation.

In a first pioneering work, Fox and Goldbourne [11] used a scanning laser vibrometer to measure the axial-symmetrical mode shapes generated on a bubble-like DEA subject to AC voltage signals. They then observed that the natural frequencies and the oscillation amplitudes associated to those mode shapes vary as functions of the electro-mechanical loads [12].

Garnell et al. carried out an extensive analysis of the vibration and acoustic response of a pneumatically biased bubble-like DEA used as a loudspeaker [13]. The authors built a structural dynamic model of the system based on a finite element (FE) formulation. They carried out experiments with a laser Doppler vibrometer, measuring a wide set of structural axial-symmetrical eigenmodes, and proved the ability of their model to predict the experimental modes. Similar to other lightweight structures [14], they demonstrated that there exists a strong coupling between the DEA membrane vibrations and the resulting air pressure waves, which is due to the low thickness, density, and stiffness of the DE membranes. Those effects were accounted for by resorting to a coupled electro-elasto-acoustic formulation [15].

Gareis et al. [16] proposed a dynamic continuum model of a buckling DEA actuator, based on the assumption of small strain and linear elastic material behaviour, and compared it with measurements of the DEA membrane central point displacements.

Whereas the mentioned works focused on axial-symmetrical deformations, experimental three-dimensional analyses of DEA structures' dynamics were also carried out [4, 9, 17] using laser scanning vibrometers. In particular, Nalbach et al. [17] measured the velocity spectra and mode shapes of a square DEA membrane deformed out-of-plane by a pulling force, and excited by an AC voltage on an annular electrode sub-portion. They hence identified a set of complex three-dimensional eigenmodes, and observed the trends in their natural frequencies as a function of the structural masses, the applied bias voltage, and the mechanical pre-load.

This paper deals with modelling and experimental characterisation of the continuum dynamics of a circular out-of-plane DEA (COP-DEA) [18]. The COP-DEA consists in an annular DEA membrane connected to a biasing elastic element, which impresses an out-of-plane deformation on the membrane and allows it to axially expand upon electrical activation. The COP-DEA is one of the most popular DEA layouts, and it has been investigated in combination with a diversity of applications, including small robots [19], volumetric pumps [20], and loudspeakers [21]. Although modelling of the static continuum

response [22] as well as the low-frequency dynamic response [23] of COP-DEAs have been widely discussed in the past, this is the first work dealing with the complex structural dynamics occurring in COP-DEAs at high frequencies.

We first present a fully-coupled continuum model for the COP-DEA dynamics, including the contribution of the electro-hyperelastic dynamics and the acoustic pressure loads. This model allows predicting the complex three-dimensional mode shapes and natural frequencies of the DE membrane, and selecting the design parameters so as to change the distribution of the natural frequencies. We then propose a lumped-parameter model for the forced DEA dynamic response. The reduced model is built using inputs from the continuum model, but it presents lower computational burden, and is therefore practical for design or control-oriented simulations.

Using a laser scanning vibrometer, we present an experimental characterisation of the vibration response of different COP-DEA geometries, subject to broadband excitation under the effect of different electro-mechanical pre-loads. In particular, we identify the mode shapes and natural frequencies of the DEAs in different working conditions, and the associated velocity spectra at different points over the membrane surface.

We then present an extensive comparison between theoretical predictions and experimental data. By resorting to a coupled FE approach, we are able to predict the different mode shapes characterising the DEA dynamics (including low-amplitude three-dimensional circumferential modes), and we show that their natural frequencies are significantly affected by the acoustic pressure loads caused by the DEA vibrations. We then show that the forced dynamics of the DEA can be efficiently described using the lumped-parameter version of the model, whose dynamic parameters are properly calibrated based on the results of the fully-coupled FE analysis.

To the author best knowledge, the present work represents one of the most extensive available analyses on the continuum dynamics of DEAs. In contrast with previous works, which focused either on eigenfrequency analyses [12, 17], or on the study of the membrane velocity time history at a target point [16], this article presents a comprehensive analysis of different aspects of the DEA continuum dynamics. These include: 1) systematic evaluation of the free-response eigenfrequencies and three-dimensional structural mode shapes, and how these are influenced by coupled electro-elasto-acoustic effects; 2) characterisation and prediction of the forced vibration response and the velocity spectra at different points over the DEA surface; 3) extensive evaluation of the influence of different design and control parameters on the DEA free and forced dynamic response. Compared to the authors' early work on lumped modelling of COP-DEA vibrations [24], this paper accounts for the effect of the acoustic loads on the structural dynamics, and presents an extensive experimental validation.

The numerical approaches validated in this work can be used to analyse the dynamics of COP-DEAs at different levels. The proposed fully-coupled three-dimensional FE analysis allows identifying suitable working ranges for the DEA where certain mode shapes should be included or avoided. The reduced model of the forced dynamics provides, in contrast, a computationally convenient tool for design and optimisation of high-frequency COP-DEA systems, or real-time control applications, such as the active shaping of the acoustic response in DEA loudspeakers.

The paper is structured as follows. Sect. 2 introduces the architecture and operating principle of the COP-DEA. Sect. 3 presents a multi-physics continuum dynamic model of the system, together with its lumped-parameter reduced versions. Sect. 4 describes the experimental setup, and presents an overview of the results. Sect. 5 presents a validation of the model, both in terms of the DEA eigenfrequencies and the velocity spectra. Finally, Sect. 6 discussed the conclusions.

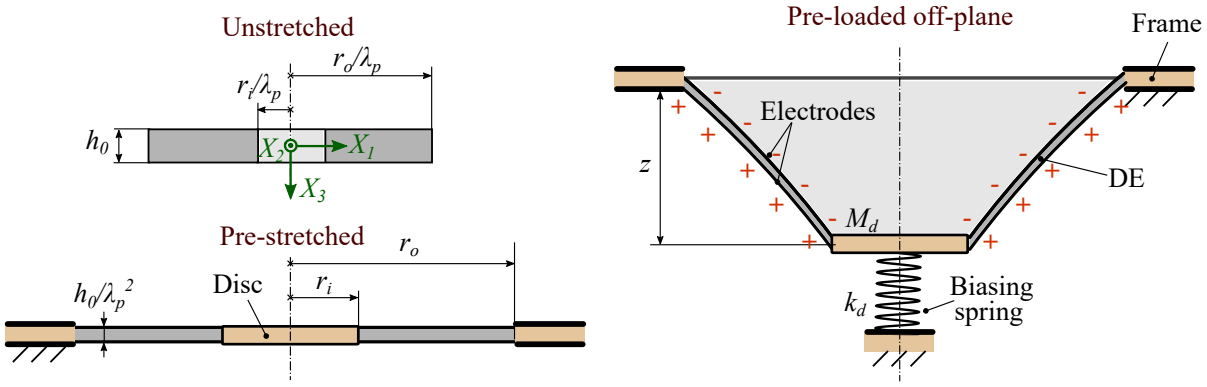

Figure 1: Layout of the COP-DEA. The DEA is built by pre-stretching a flat annular membrane (top left), clamping its edges to a rigid solid disc and an annular outer frame (bottom left), and deforming it out-of-plane via a biasing element (right).

2 Circular out-of-plane DEA

The COP-DEA [18, 23] is made of a planar annular DE membrane, holding deformable electrodes on both surfaces. The membrane has its outer perimeter attached on a fixed frame, and the inner perimeter connected to a rigid disc. The inner disc is free to move along the axis, and it is connected to a pre-loaded mechanical biasing element (e.g., a spring) which impresses an initial out-of-plane conical-like deformation to the DEA membrane (see Fig. 1). In the flat configuration, prior to the application of the elastic biasing element, the membrane is subject to an equibiaxial pre-stretch λ_p. We denote as r_i and r_o the inner and outer radii of the pre-stretched membrane, respectively, while z represents the equilibrium distance between the central disc and the outer frame, and h_0 describes the DE thickness in the undeformed state (before pre-stretching). Assuming the DE material incompressible [25], the thickness of the membrane in the pre-stretched configuration is h_0/λ_p^2.

When a voltage difference is applied between the electrodes, the DE membrane further expands out-of-plane and the axial distance z of the central disc and the outer perimeter increases. Notice that, if no mechanical biasing was present ($z = 0$), the COP-DEA could not produce any out-of-plane displacement of the central disc, since the stresses acting on the membrane would entirely lie in-plane. Namely, the state corresponding to $z = 0$ is a singular configuration for the actuator.

Although at low frequencies the COP-DEA motion is pistonic, i.e., dominated by axial displacements of the membrane and the disc, in the presence of high frequencies or broadband voltage excitations the COP-DEA exhibits complex dynamics, characterised by combined radial and axial deformations of the membrane profile. In our previous work [24], we observed that, in case the mass of the central disc is much larger than the membrane mass, the motion of the COP DEA at high frequencies entirely consists of structural deformations of the membrane profile, with no motion of the central disc.

Knowledge of high order structural dynamics, as well as the frequencies at which they are triggered, is crucial as it either 1) allows identifying upper bounds for the working range of devices exploiting a purely pistonic motion; or 2) enables design and optimisation of applications that could exploit such complex structural dynamics, e.g., loudspeakers [24].

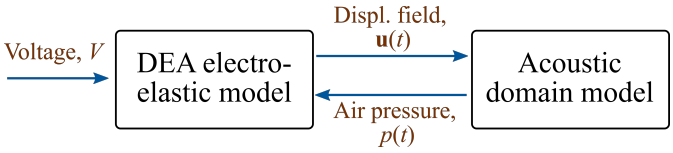

Figure 2: Block-diagram structure of the coupled model.

3 Multi-domain dynamic model of COP DEAs

In this section, we present a multi-domain model for the continuum dynamics of COP-DEAs. The dynamics of the DEA is described by taking into account two main multi-physics interactions:

- Electro-mechanical interactions, i.e., the contribution of the electric stresses (namely, the Maxwell stress) on the DEA dynamics
- Interaction between acoustic domain and structure, i.e., the effect of the air pressure variations induced by structural vibrations of the DE membrane on the DEA dynamics

Whereas electro-mechanical coupling in DEs has been largely studied and is key to the description of the working principle of any DEA system, the interaction with the acoustic domain has been recently found to play an important role in the structural vibrations of DEAs operating at high frequencies [15]. In fact, the air pressure gradients (namely, the acoustic waves) induced by the vibrations of thin lightweight membranes (such as DEs) generate loads that are comparable to the membrane inertial forces, and play an important role in the dynamic response of the structure [14].

We first present a general formulation for the fully-coupled problem, which combines structural, electrostatic, and acoustic domains. We then present a reduced model, built upon calibration data from experiments and dynamical parameters computed using the fully-coupled continuum model, which allow describing the complex COP-DEA dynamics in a simplified computationally-convenient way, thus making it suitable for iterative design and control applications.

3.1 Fully-coupled three-dimensional model

We hereby present a fully-coupled model with the structure shown in Fig. 2 , which includes: 1) a continuum electro-elastic model of the DEA; and 2) the response of the surrounding acoustic domain. The electro-elastic model uses the time-varying applied voltage as the input, and computes the time-history of the displacements of points on the membrane surface. The latter represent an input to the acoustic model, which computes the air pressure loads on the membrane, which are fed back into the DEA model.

The continuum DE dynamic model relies on the following assumptions:

- The DE membrane is a thin shell element, with negligible bending stiffness. Stretches and stresses are constant through the thickness, and no stress acts in the thickness direction (plane-stress).
- The DE material can be described as an incompressible visco-hyperelastic continuum [25]. The mechanical response of the electrodes is not modelled explicitly, and it is indirectly accounted for through a suitable choice of the elastic parameters.
- In the presence of an electric potential difference between the electrodes, the DE material behaves as an ideal dielectric. Electrical loses due to the electrodes resistivity and the DE conductivity [26] are here neglected.

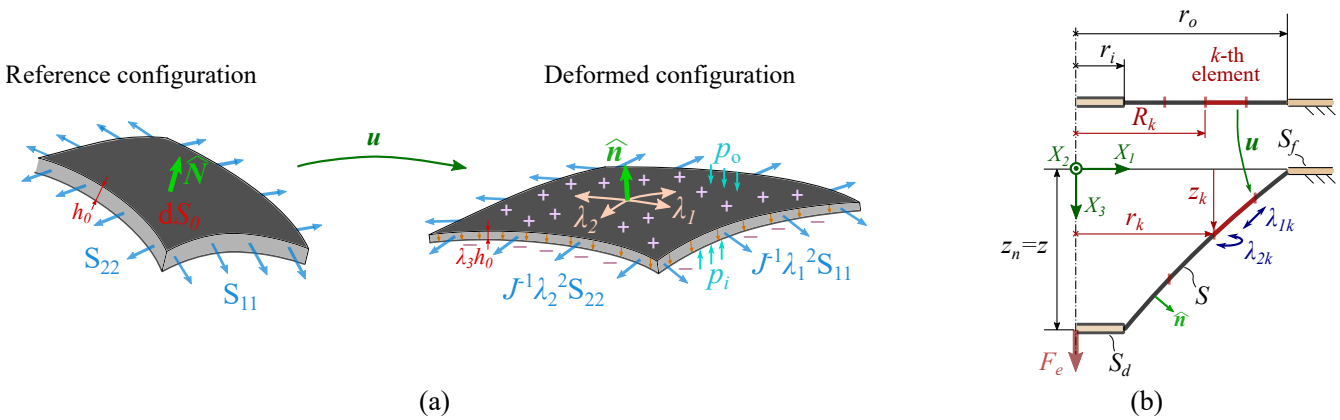

Figure 3: (a) DE membrane element in the undeformed state (left part) and in the stretched state, subject to displacement $\mathbf{u}$ (right part). (b) COP-DEA discretisation into annular portions.

We consider a generic three-dimensional membrane element (Fig. 3a), and we call $\mathbf{u} = \mathbf{u}(\mathbf{X}, t)$ the displacement functions that maps a material point $\mathbf{X}$ on the undeformed membrane into a spatial point $\mathbf{x}$: $\mathbf{x} = \mathbf{X} + \mathbf{u}(\mathbf{X}, t)$. We define $\mathbf{F} = \text{Grad}\ \mathbf{u}$ the deformation gradient (with Grad denoting the material-frame gradient operator) and $\mathbf{C} = \mathbf{F}^T\mathbf{F}$ the right Cauchy-Green tensor. The square-rooted eigenvalues of $\mathbf{C}$ represent the membrane principal stretches, and they are denoted λ_1, λ_2 and λ_3. Owing to incompressibility, the following equality holds:

$$\lambda_1\lambda_2\lambda_3 = 1. \tag{1}$$

In thin membranes, the thickness direction is a principal deformation direction. If the membrane is in tension, the minimum stretch λ_3 represents the stretch along the thickness, whereas λ_1 and λ_2 are tangential in-plane stretches. Because of the thin membrane assumption, elements $\mathrm{C}_{3,1}$ and $\mathrm{C}_{3,2}$ (and their symmetric counterparts) of $\mathbf{C}$ are equal to 0.

We formulate the equation of motion of the deformed membrane in terms of material coordinates in the undeformed frame. With the aim of including the contribution of the air pressure loads directly into the equation of motion, we consider the dynamics' equation of the DE membrane element expressed in weak form [27]:

$$h_0 \int_{S_0} (\mathbf{F}\ \mathbf{S}) : \text{Grad}\boldsymbol{\eta}\ \mathrm{d}S_0 + \int_{S_0} J p_\delta \mathbf{F}^{-T}\hat{\mathbf{N}} \cdot \boldsymbol{\eta}\ \mathrm{d}S_0 - \rho_0 h_0 \int_{S_0} \ddot{\mathbf{u}} \cdot \boldsymbol{\eta} \mathrm{d}S_0 = 0 \tag{2}$$

where h_0 and ρ_0 are the initial membrane thickness and density (assumed uniform); $\ddot{\mathbf{u}}$ is the material points' acceleration with respect to the reference configuration; $\hat{\mathbf{N}}$ is a unit vector perpendicular to the undeformed membrane surface; J is the determinant of $\mathbf{F}$; $p_\delta = p_o - p_i$ is the air pressure difference between the two faces of the membrane (with p_o being the pressure on the external face, towards which the normal points); $\mathbf{S}$ is the second Piola-Kirchoff stress tensor. Because of the thin membrane assumption, elements $\mathrm{S}_{\mathrm{i},3}$, $\mathrm{i} = 1, 2, 3$ (and their symmetric counterparts) are equal to 0. Finally, $\boldsymbol{\eta}$ is a generic test function (namely, a virtual displacement) satisfying the boundary conditions. Operator : is the tensor double-dot product, and $\cdot$ is a scalar product. Integrals in (2), are calculated over the reference membrane surface, denoted by S_0.

In the case of the COP-DEA, we consider a material reference frame (X_1, X_2, X_3) centred on the device axis, with axes X_1 and X_2 on the undeformed membrane plane, and the third axis X_3 parallel to the thickness (Fig. 1). Assuming that the central rigid disc can only move axially, the following boundary

conditions hold:

$$\begin{cases} u_i|_{\Gamma_o} = (\lambda_p - 1)X_i, \ i = 1,2, \ u_3|_{\Gamma_o} = 0 \\ u_i|_{\Gamma_i} = (\lambda_p - 1)X_i, \ i = 1,2 \\ \left[\mathbf{FS}\hat{\mathbf{N}}\Big|_{\Gamma_i}\right]_3 = \dfrac{\lambda_p}{2\pi r_i h_0} F_e \end{cases} \tag{3}$$

where $\Gamma_o = \{(X,Y) : X^2 + Y^2 = r_o^2/\lambda_p^2\}$ and $\Gamma_i = \{(X,Y) : X^2 + Y^2 = r_i^2/\lambda_p^2\}$ are the sets of points on the outer and the inner perimeter respectively; u_i are the components of $\mathbf{u}$. The first two conditions express the displacement of the points on the membrane outer and inner perimeter respectively due to pre-stretch. The last condition accounts for the force F_e applied by the biasing element on the membrane:

$$F_e = k_b(\, u_3|_{\Gamma_o} - l_b) + M_d \ddot{u}_3 \tag{4}$$

where k_b and l_b describe the stiffness and the preload of the biasing element (here, a linear spring), and M_d is the central disc mass.

Conditions (3) hold in case the mass of the biasing spring is negligible. If such a mass is comparable to M_d, further considerations are required to incorporate the spring continuum dynamics into the formulation (see Annex I).

3.1.1 Electro-visco-elastic constitutive model

Stress tensor $\mathbf{S}$ is symmetric, and can be expressed as a sum of terms as follows [25]:

$$\mathbf{S} = \mathbf{S}_{em}(\mathbf{C}, V) - \gamma \mathbf{C}^{-1} + \mathbf{S}_v(\mathbf{C}, \gamma_1, \ldots, \gamma_m), \tag{5}$$

where $\mathbf{S}_{em}$ is an electro-elastic equilibrium stress, which is a function of $\mathbf{C}$ and the voltage on the electrodes; the second term accounts for the material incompressibility: in particular, γ is an indefinite multiplier, whose value is resolved by prescribing the plane stress assumption; $\mathbf{S}_v$ is a non-equilibrium stress, which accounts for the dissipative response of the material, and it is a function of $\mathbf{C}$ and a set of strain-like variables $\gamma_1, \ldots, \gamma_m$ describing the internal visco-elastic dynamics.

Constitutive relationships for $\mathbf{S}_{em}(\mathbf{C}, V)$ are formulated in terms of an electro-mechanical co-energy function $\Psi_{em} = \Psi_{em}(\mathbf{C}, V)$, such that:

$$\mathbf{S}_{em} = 2\frac{\partial \Psi_{em}(\mathbf{C}, V)}{\partial \mathbf{C}}. \tag{6}$$

where $V = V(t)$ is the voltage applied on the electrodes, which is the system input variable. For a thin single-layer membrane with electrodes on the outer faces, Ψ_{em} can be written as:

$$\Psi_{em}(\mathbf{C}, V) = \Psi_m(\mathbf{C}) - \frac{\varepsilon}{2}\left(\frac{V}{h_0}\right)^2 \frac{J(\mathbf{C})}{\mathrm{C}_{33}}. \tag{7}$$

The first term on the right-hand side of (7) is the elastic strain-energy function, expressing the elastic energy density of the elastomer as a function of the stretches, according to a given hyperelastic model [28]. The second term on the right-hand side of (7) represents a generalised electrostatic potential energy contribution (or co-energy), equal to the energy supplied to the DE by the power supply minus the electrostatic potential energy [18]. In particular, ε is the DE permittivity, and J is the determinant of $\mathbf{F}$.

The non-equilibrium stress can be formulated resorting to established visco-elastic models, which make use of a set of additional equations for the internal states dynamics [29]. In the results presented in this work (see Sect. 5), we describe the structural damping in a simplified way, making use of an experiment-based identification, without explicit use of a visco-elastic model. Further details on visco-elastic constitutive relationships for $\mathbf{S}_v$ are hence omitted.

3.1.2 Acoustic-structure interaction

We consider a DE membrane immersed in an open infinite air volume, i.e., the membrane has air on both faces. In case a low thickness DE membrane is considered, the pressure waves caused by the membrane motion might have a significant impact on the structure dynamics [15].

We consider a spatial reference frame, describing the geometry of the static deformed equilibrium position of the DE membrane. For the acoustic problem, we assume that the system geometry is simply composed of the deformed membrane surface, the central rigid disc, and the outer frame, which are all rendered as thin flat surfaces (S, S_d, and S_f respectively - see Fig. 3). The air pressure distribution, denoted by $p(\mathbf{x}, t)$, is described by the Helmholtz equation and the following boundary conditions:

$$\begin{cases} \dfrac{\partial^2 p}{\partial t^2} = c_a^2 \mathrm{div}\,(\mathrm{grad}\ p) \\ \rho_a \hat{\mathbf{n}} \cdot \mathrm{grad}\ p_o|_{S \cup S_d} = -\hat{\mathbf{n}} \cdot \dfrac{\partial^2 \mathbf{u}}{\partial t^2} \\ \rho_a \hat{\mathbf{n}} \cdot \mathrm{grad}\ p_i|_{S \cup S_d} = \hat{\mathbf{n}} \cdot \dfrac{\partial^2 \mathbf{u}}{\partial t^2} \\ \hat{\mathbf{n}} \cdot \mathrm{grad}\ p_o|_{S_f} = 0 \\ \hat{\mathbf{n}} \cdot \mathrm{grad}\ p_i|_{S_f} = 0 \end{cases} \tag{8}$$

where div and grad represent the spatial divergence and gradient operators; c_a is the sound speed in air; ρ_a is the air density; $\hat{\mathbf{n}}$ is the normal vector to the geometry's surfaces (deformed DEA, fixed frame, rigid disc). The first two boundary conditions express the continuity of the velocity between the air and the moving DEA sruface ($S \cup S_d$), whereas the last two conditions account for the fixed perfectly-reflecting frame surface (S_f). A discontinuity on p is present in correspondence of the surfaces, hence p_o and p_i represent the values of the pressure evaluated respectively on the outer faces (where $\hat{\mathbf{n}}$ is pointing) and the inner faces of the geometry's surfaces (see also Eq. (2)).
In contrast with Eq. (2), Eq. (8) makes use of a spatial representation, i.e., the accelerations and gradients are expressed in terms of the coordinates of the deformed geometry. Notice also that Eq. (8) is linear, provided that surfaces S and S_d are fixed and correspond to the static equilibrium surfaces of the deformed DEA.

3.1.3 Modal shapes analysis

Combining Eqs. (2)-(8) provides a model that relates the membrane displacement field $\mathbf{u}$ with the input voltage V. Such a model allows identifying a set of three-dimensional mode shapes (including non-axial-symmetrical modes) that describe the free linearised response of the COP-DEA in the neighbourhood of an equilibrium configuration, where the DEA is subject to the biasing spring load and a constant voltage bias $V = V_b$.

We call $\mathbf{u}_0$ the static deformation of the system, which is subject to constant voltage V_b and boundary conditions (3), i.e., $\mathbf{u} = \mathbf{u}_0$ and $\ddot{\mathbf{u}} = \dot{\mathbf{u}} = 0$ is a solution of Eq. (2). Linearising Eqs. (2)-(8) with respect to $\mathbf{u}$ around $\mathbf{u}_0$ and researching a solution to the equation system in the form $\mathbf{u} = \mathbf{u}_0(\mathbf{X}) + \tilde{\mathbf{u}}_k(\mathbf{X}) \exp(i\omega_k t)$

provides an eigenvalue problem (whose explicit equation is here omitted for simplicity). The solution to the eigenvalue problem provides a set of natural frequencies ω_k and the corresponding mode shape profiles $\tilde{\mathbf{u}}_k$, which represent displacements with respect to the equilibrium pre-loaded position.

Considering the whole set of Eqs. (2)-(8) provides a set of mode shapes that account for the coupled acoustic-structural response of the DEA. Qualitatively, the acoustic loads generated by a structure vibrations provide the structure with an added mass and a radiation damping, which are respectively due to the air kinetic energy and the radiated acoustic waves [30]. Such additional mass and damping generally depend on the oscillation frequency, and they might affect the system dynamics in those working regimes where the moving structural mass or the damping are comparable to the acoustic mass and damping.

3.2 Reduced model of the forced axial-symmetrical response

If electrodes cover the whole DEA surface, the system is practically axial-symmetric. In this case, non-axial-symmetrical steady-state deformation patterns in the forced dynamics can only be explained in terms of local inhomogeneities or higher order effects (e.g., minor asymmetries and inhomogeneities in the boundary conditions). Since these effects are difficult to systematically model, and are also expected to play a minor role in the forced system dynamics, we hereby propose a reduced axial-symmetrical lumped-parameter version of the general model presented in Sect. 3.1, suitable to describe the forced dynamics of the COP-DEA in the presence of small-amplitude voltage excitation. Due to its computational simplicity, the proposed reduced model can be used as a convenient reference for the design of applications and driving strategies.

On this end, we first introduce a finite-dimensional lossless axial-symmetrical reduced version of the COP-DEA structural dynamics (excluding the contribution of the acoustic pressure). Based on that, we then reformulate the DEA equations of motion via a linear modal decomposition approach. Finally, we introduce simplified damping and acoustic added mass terms in a simplified fashion, directly into the modal form of the equations of motion.

3.2.1 Finite-dimensional lossless structural model formulation

A finite-dimensional axial-symmetrical model for the structural dynamics of the COP-DEA (excluding the contribution of the acoustic coupling) can be obtained by ideally dividing the DE membrane into ring elements. This approach has been introduced by the authors of this paper in [24], and is shortly recalled in the following.

Let us ideally partition the flat pre-stretched DEA into n concentric elements, and call R_k the inner radius of the $k-$th element in the flat pre-stretched configuration ($k = 1$ indicates the outer element, with external diameter r_o, while $k = n$ denotes the inner element, with internal diameter $r_n = r_i$), as shown in Fig. 3b. Let us then call r_k and z_k the radial and axial positions of the inner radius of the $k-$th element in a deformed state. The surface (meridian and circumferential) stretches λ_{1k} and λ_{2k} on the $k-$th element in the meridian, circumferential and thickness direction respectively read as:

$$\lambda_{1k} = \lambda_p \frac{\sqrt{(r_k - r_{k-1})^2 + (z_k - z_{k-1})^2}}{R_{k-1} - R_k}, \ \lambda_{2k} = \lambda_p \frac{r_k + r_{k-1}}{R_{k-1} + R_k} \tag{9}$$

and the stretch λ_{3k} in the thickness direction relates to the these via Eq. (1)

Denoting $\mathbf{q} = [r_1, \dots, r_{n-1}, z_1, \dots, z_n]^\intercal$ a vector of generalised coordinates (where $z_n = z$, as defined in Fig. 1), the equations of motion of the DEA can be written in a lagrangian fashion as follows:

$$\frac{\mathrm{d}}{\mathrm{d}t} \frac{\partial T(\dot{\mathbf{q}})}{\partial \dot{\mathbf{q}}} + \frac{\partial U_m(\mathbf{q})}{\partial \mathbf{q}} - \frac{V^2}{2} \frac{\partial C(\mathbf{q})}{\partial \mathbf{q}} = \mathbf{0}, \tag{10}$$

where T is the device kinetic energy; U_m is the elastic potential energy; the third term represents a generalised electrostatic potential energy (similar to Eq. (7) [18]); and C_d in the total DEA capacitance, namely:

$$C_d = \sum_{k+1}^{n} C_k, \text{ with } C_k = \frac{\pi^2 \varepsilon (r_k + r_{k+1})^2 \left((r_k - r_{k-1})^2 + (z_k - z_{k-1})^2 \right)}{\Omega_k}, \tag{11}$$

where $\Omega_k = \pi(R_{k-1}^2 - R_k^2)t_0/\lambda_p^2$ is the volume of the $k-$th element.

The kinetic energy is the sum of the kinetic energies of the single elements T_k $(k = 1, \ldots, n)$ plus the energy of the central disc:

$$T = \sum_k T_k + \frac{1}{2} M_b \dot{z}^2, \; T_k = \pi \rho_0 \frac{h_0}{\lambda_p^2} \int_{R_k}^{R_{k-1}} \left(v_{rk}^2(R) + v_{zk}^2(R) \right) R \, \mathrm{d}R \tag{12}$$

where v_{rk} and v_{zk} are radial and axial velocity distributions such that: $v_{rk}(R_{k-1}) = \dot{r}_{k-1}$, $v_{rk}(R_k) = \dot{r}_k$, $v_{zk}(R_{k-1}) = \dot{z}_{k-1}$, $v_{zk}(R_k) = \dot{z}_k$, and they are assumed to vary linearly with R. Note that the kinetic energy of the biasing spring is neglected by (12). An extended formulation which accounts for its contribution in the dynamics is given in Annex I.

The elastic energy is the sum of the elastic energy of the membrane rings and the elastic energy of the biasing spring:

$$U_m = \sum_{k=1}^{n} \Omega_k \tilde{\Psi}_m(\lambda_{1k}, \lambda_{2k}, \lambda_{3k}) + \frac{1}{2} k_b \left(l_b - z \right)^2, \tag{13}$$

where $\tilde{\Psi}_m$ is the elastic strain-energy function (see Eq. (7)), rewritten as a function solely of the principal stretches [25].

Notice that Eqs. (9)-(12) hold for all $k = 1, \ldots, n$ with the following observations: for $k = 1$, $R_{k-1} = r_{k-1} = r_o$ and $z_{k-1} = 0$; for $k = n$, $R_k = r_k = r_i$.

Eq. (10) is a set of $2n - 1$ non-linear dynamic equations. We hereby consider small vibrations of the DEA generated by small-amplitude time-dependent voltage perturbations, namely: $V(t) = V_b + \tilde{V}(t)$, with $|\tilde{V}(t)| \ll V_b$. Under this assumption, we can linearise Eq. (10) and express it as follows:

$$\begin{aligned} &\mathbf{M}_s \ddot{\tilde{\mathbf{q}}} + \mathbf{K}_s \tilde{\mathbf{q}} = \mathbf{d}(t), \text{ with } \mathbf{M}_s = \left(\frac{\partial^2 T(\dot{\mathbf{q}})}{\partial \dot{\mathbf{q}}^2} \right)_{\dot{\mathbf{q}}=0}, \\ &\mathbf{K}_s = \left(\frac{\partial^2 U_m(\mathbf{q})}{\partial \mathbf{q}^2} \right)_{\mathbf{q}=\mathbf{q}_0} - \frac{V_b^2}{2} \left(\frac{\partial^2 C(\mathbf{q})}{\partial \mathbf{q}^2} \right)_{\mathbf{q}=\mathbf{q}_0}, \; \mathbf{d}(t) = 2 V_b \tilde{V}(t) \left(\frac{\partial C(\mathbf{q})}{\partial \mathbf{q}} \right)_{\mathbf{q}=\mathbf{q}_0} \end{aligned} \tag{14}$$

where $\mathbf{M}_s$ and $\mathbf{K}_s$ are mass and stiffness matrices, $\mathbf{q}_0$ such that $\ddot{\mathbf{q}}_0 = \dot{\mathbf{q}}_0 = 0$ is the equilibrium state corresponding to $V(t) = V_b$, $\tilde{\mathbf{q}} = \mathbf{q} - \mathbf{q}_0$ is the deviation from the equilibrium state, and $\mathbf{d}$ is the voltage-induced excitation.

3.2.2 Modal decomposition and truncation

Based on Eq. (14), the natural frequencies and mode shapes of the undamped acoustically uncoupled system can be found by solving:

$$\mathbf{K}_s \hat{\mathbf{q}}_k = \omega_k^2 \mathbf{M}_s \hat{\mathbf{q}}_k, \; k = 1, \ldots, 2n - 1 \tag{15}$$

where ω_k is the $k-$th natural frequency of the system, and $\hat{\mathbf{q}}_k$, with $k + 1, \ldots, 2n - 1$ are a set of mode shape profiles, which can be chosen in such a way that the following generalised orthogonality properties

apply [31]:

$$\mathbf{Q}_\alpha^T \mathbf{M}_s \mathbf{Q}_\alpha = \mathbf{M}_{s,\alpha} = \mathrm{diag}(m_{\alpha,1}, \ldots, m_{\alpha,2n-1}),\ \mathbf{Q}_\alpha^T \mathbf{K}_s \mathbf{Q}_\alpha = \mathbf{K}_{s,\alpha} = \mathrm{diag}(k_{\alpha,1}, \ldots, k_{\alpha,2n-1}), \tag{16}$$

where $\mathbf{Q}_\alpha = [\hat{\mathbf{q}}_1, \ldots, \hat{\mathbf{q}}_{2n-1}]$ is the modal matrix; $m_{\alpha,k}$ and $k_{\alpha,k}$ are called modal mass and stiffness coefficients such that $k_{\alpha,k}/m_{\alpha,k} = \omega_k^2$. $\mathbf{M}_s$ and $\mathbf{K}_s$ can be proven to be symmetric and positive definite, hence guaranteeing that all ω_k are real and that Eq. (16) holds [31]. In practice, the eigenvectors $\hat{\mathbf{q}}_k$ can be conveniently normalised in such a way that $m_{\alpha,k} = 1\ \forall\ k$ [32].

Generalised coordinates $\tilde{\mathbf{q}}$ can be expressed as linear superposition of mode shapes, namely $\tilde{\mathbf{q}} = \mathbf{Q}_\alpha \boldsymbol{\alpha}$. The new configuration variable $\boldsymbol{\alpha}$ is called the modal representation of $\tilde{\mathbf{q}}$, and allows reformulating Eq. (14) in a modal fashion, as follows [33]:

$$\mathbf{M}_{s,\alpha} \ddot{\boldsymbol{\alpha}} + \mathbf{K}_{s,\alpha} \boldsymbol{\alpha} = \mathbf{d}_\alpha(t),\ \text{with}\ \mathbf{d}_\alpha(t) = \mathbf{Q}_\alpha^T \mathbf{d}(t). \tag{17}$$

If n is sufficiently large (i.e., ω_k is above the frequencies of interest for some k), $\tilde{\mathbf{q}}$ can be tightly approximated as the sum of a subset of l mode shapes (with $l < 2n-1$), i.e., $\tilde{\mathbf{q}} = \mathbf{Q}_\alpha \boldsymbol{\alpha} \approx \bar{\mathbf{Q}}_\alpha \bar{\boldsymbol{\alpha}}$, where $\bar{\boldsymbol{\alpha}}$ is the truncated representation of $\boldsymbol{\alpha}$ while $\bar{\mathbf{Q}}_\alpha$ is an $(2n-1) \times l$ modal matrix containing a sub-set of l columns of $\mathbf{Q}_\alpha$. Each one of the columns of $\bar{\mathbf{Q}}_\alpha$ represents a different modal shape. The first l modes, or a selected set of l modes which are relevant to the problem under investigation, represent suitable choices for the model truncation. The corresponding reduced modal mass and stiffness matrices $\bar{\mathbf{M}}_{s,\alpha}$ and $\bar{\mathbf{K}}_{s,\alpha}$ are computed accordingly, by considering a subset of the elements of the corresponding $\mathbf{M}_{s,\alpha}$ and $\mathbf{K}_{s,\alpha}$ matrices. Under the above considerations, Eq. (17) can be effectively truncated as follows:

$$\bar{\mathbf{M}}_{s,\alpha} \ddot{\bar{\boldsymbol{\alpha}}} + \bar{\mathbf{K}}_{s,\alpha} \bar{\boldsymbol{\alpha}} = \bar{\mathbf{d}}_\alpha(t),\ \text{with}\ \bar{\mathbf{d}}_\alpha(t) = \bar{\mathbf{Q}}_\alpha^T \mathbf{d}(t). \tag{18}$$

Because of condition (16), Eq. (18) represents a set of decoupled linear equations.

3.2.3 Reduced model

The contribution of structural damping and acoustic added mass can be introduced into Eq. (18) in a simplified manner.

By assuming that the damping and the acoustic loads are small compared to the structural, inertial, and electrostatic loads, the following practical simplifications can be introduced:

- In the presence of visco-elastic damping and acoustic pressures, the mode shapes of the DEA are the same as in the undamped "dry" scenario in the absence of acoustic loads (see Eq. (15)).
- The contribution of the acoustic and viscous material damping loads can be approximately accounted for in Eq. (18) via additional linear and time-invariant diagonal damping and inertial terms. Notice that, assuming a diagonal damping matrix in the modal reduced form is in fact equivalent to resorting to a proportional damping model [34].

We thus introduce the following modal-domain equation of motion for the damped DEA in air:

$$\left(\bar{\mathbf{M}}_\alpha + \bar{\mathbf{M}}_{ad}\right) \ddot{\bar{\boldsymbol{\alpha}}} + \bar{\mathbf{B}}_\alpha \dot{\bar{\boldsymbol{\alpha}}} + \bar{\mathbf{K}}_\alpha \bar{\boldsymbol{\alpha}} = \bar{\mathbf{d}}_\alpha(t), \tag{19}$$

where $\bar{\mathbf{M}}_{ad}$ and $\bar{\mathbf{B}}_\alpha$ are matrices accounting for the air added mass and the total damping (which is the sum of an acoustic and a structural contribution).
Compared to an exact fluid-structural coupled model, the present formulation makes use of time-invariant

acoustic added mass coefficients, neglecting their dependency on the frequency [30]. In practice, this assumption hold if the individual modes have a rather narrow band, which is in fact consistent with the experimental observations described in the following (see Sect. 4.3). Although model (19) builds upon the assumption that the system mode shapes are the same as in the dry undamped case, the additional aerodynamic inertia introduced causes a shift in the natural frequencies of the modes.

The terms $\bar{\mathbf{M}}_\alpha$, $\bar{\mathbf{K}}_\alpha$ and $\bar{\mathbf{d}}_\alpha$ in Eq. (19) can be analytically derived based on the discretised model presented in Sects. 3.2.1 and 3.2.2. The additional terms $\bar{\mathbf{M}}_{ad}$ and $\bar{\mathbf{B}}_\alpha$, instead, can be calibrated a-posteriori based on experimental observations, or calculated with dedicated analyses. In this paper (Sect. 5) we explicitly solve the fully-coupled eigenvalue problem (Sect. 3.1.3) using a FE approach, and we use the resulting estimate of the natural frequencies to compute $\bar{\mathbf{M}}_{ad}$, whereas we calibrate the damping based on a restricted set of experimental measurements.

Compared with a fully-coupled continuum formulation, which involves complex visco-elastic models that are difficult to calibrate within a broad frequency range, this formulation allows including the contribution of damping through a reduced number of parameters that directly map into the modal response of the DEA, and can be conveniently employed for design and control purposes, leading to a significant reduction in the computational burden.

4 Experimental characterisation

This section presents the setup and results of a set of experimental tests aimed at characterising the continuum dynamics of COP-DEAs. The response of the device is characterised in terms of the mode shapes, their natural frequencies, as well as the velocity spectra of a set of target points on the COP-DEA when the latter is subject to a broadband frequency excitation.

4.1 COP-DEA samples

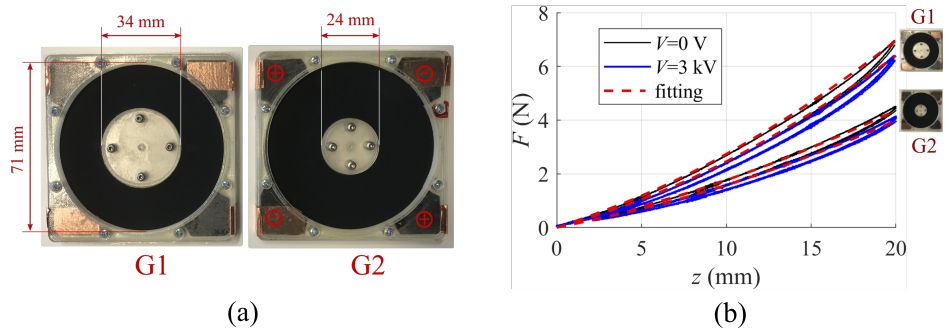

Figure 4: (a) Picture of the COP-DEA samples used for the tests. (b) Force vs. central disc displacement response (at 0 and 3 kV) for the COP-DEA samples measured via tensile tests.

We manufactured COP-DEA samples made of DE silicone Elastosil 2030 by Wacker Chemie, with screen-printed carbon-loaded silicone electrodes. The composition and properties of our screen printed electrodes are described in [35]. The DE membrane samples had a pre-stretch $\lambda_p = 1.20$, and initial thickness of the dielectric layer (prior to pre-stretch) $h_0 = 100$ μm. Such a thickness represents a practical trade-off between very thin membranes, for which a solid perimeter clamping (crucial in vibration analyses) is difficult to achieve, and thick membranes, which would require very large driving voltages. The outer

rigid frame holding the membrane and the central rigid disc were 3D printed with rigid acrylic plastic. Connections of the electrodes to the power electronics were realised via copper tape foils located at the four corners of the frame (two tracks per electrode). A linear tension spring with mass $M_s = 1.8$ g, initial length $L_s = 30$ mm, and stiffness $k_d = 52$ N/m was connected to the central disc and used as the mechanical biasing element.

r_o	35.5 mm	ρ_0	1490 kg/m^3
λ_p	1.2	h_0	100 μm
k_d	52 N/m	M_s	1.8 g
L_s	30 mm	ε	$2.8 \cdot 8.85 \cdot 10^{-12}$ F/m
r_i	17 mm (G1)		12 mm (G2)
M_d	3.0 g (G1)		1.9 g (G2)

Table 1: Properties of the COP-DEA samples

Two different DEA geometries (hereafter called G1 and G2) have been tested, as shown in Fig. 4a, which have the same outer radius r_o and differ in terms of the aspect ratio r_o/r_i. A list of the samples properties is shown in Tab. 1. The density of the membrane (reported to the nominal thickness h_0) has been obtained from the actual measured membranes mass (measured with a high precision scale), and it thus includes the contribution of the electrodes' mass as well. The dielectric permittivity is given by the DE material datasheet [36].
Tensile tests at voltages between 0 and 3 kV (i.e., the voltage ranges used in the tests) have been preliminarily done on the membranes to measure their force-displacement characteristic (Fig. 4b). The tensile tests were carried out on a sensorised setup available at Saarland University premises and described, e.g., in [37]. As expected, geometry G1 has a larger total stiffness (i.e., the slope of the force-displacement response), because, given the same value of the disc axial displacement z, it is subject to larger meridian stretch along the membrane slant height. Similar to other membrane DEA topologies [29, 38], the slope of the force-displacement curves (i.e., the total actuator stiffness) decreases when a voltage is applied on the electrodes, as a result of the electrostatic force contribution.

4.2 Setup and procedures

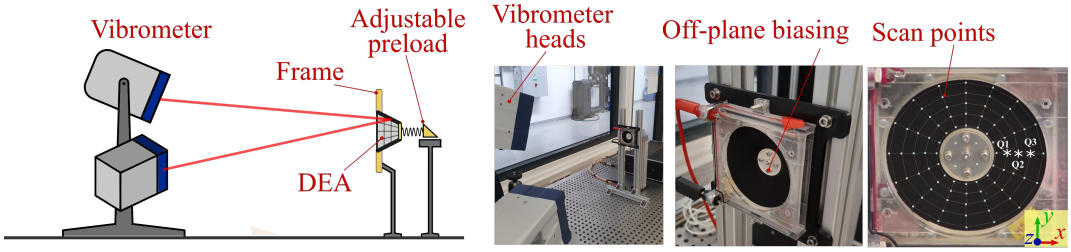

Figure 5: Schematic (a) and photo (b) of the experimental test-bench. (c) COP-DEA sample in the mounting configuration. (d) Distribution of the measurement points.

The vibration measurements are performed by using a 3D Doppler laser vibrometer PSV-500 3D by Polytec, in the same fashion as in [17]. The vibrometer has three laser heads that allow measuring the velocity components of target points on the device surface.

The DE samples are mounted in a vertical position, aligned with the vibrometer heads through a rigid structure. The out-of-plane deformation is adjusted via a positioning stage that allows controlling the spring pre-load. A schematic of the test-bench is shown in Fig. 5a, whereas pictures of a DEA sample (G2) mounted on the setup are shown in Fig. 5b,c.

The DEAs' voltage is driven via high-voltage amplifier Trek 609E-6. Data acquisition is performed by the vibrometer's proprietary software PSV 9.1. Velocity measurements are taken on a grid of 84 points (see Fig. 5d): 80 points on the DEA electrode surface and 4 points on the rigid disc.
The vibrometer scans the different points in sequence, by providing the amplifier with a selected multi-chromatic driving signal (see Supplementary Material video). The output of the measurements are the velocity spectra (for the single points and averaged over the membrane), and a 3D imaging of the membrane velocity distribution at the different frequencies.

The membrane is driven using a chirp input voltage with constant-magnitude spectrum, with a time-domain amplitude of $\tilde{V} = 100$ V, bias V_b between 1000 and 3000 V, and frequency varying from 0 and 1000 Hz. As observed in Sect. 4.3, the selected frequency range allowed observing a rather large set of mode shapes and different vibration regimes. For each scanning point, the chirp voltage signal has been applied for a time of 800 ms, using a sample time of 0.4 ms. Frequency spectra with 800 samples (resolution of 1.25 Hz) were generated.

For each of the reference DEA geometries (Fig. 4), different tests have been performed by varying: 1) the out-of-plane deformation z; and 2) the voltage bias V_b.

4.3 Results

In the following, an overview of the results obtained in the tests is presented.
Attention is first of all focused on the mean spectra (averaged on the scanning grid points) of the velocity components in the three directions (as defined by the reference frame in Fig. 5d), as provided by the vibrometer acquisition software. Spectra are computed as the fast Fourier transform (FFT) of the measured velocity, normalised by the number of frequency samples [39]. Analysing the average spectra allows us to easily detect the natural frequencies of the system and the corresponding mode shapes.

Fig. 6 shows the average spectra of DEA G1 (as defined in Fig. 4a) in the presence of a voltage bias $V_b = 2$ kV and different values of the initial out-of-plane deformation z. In the case $z = 0$, the DE membrane is flat, and no biasing element is applied on the rigid disc, whereas in the other cases the DEA is deformed by means of the pre-loaded spring.
The frequency response of the actuator is characterised by different peaks, corresponding to the system resonances. The visible peaks have a narrow band (namely, a large quality factor) and represent highly underdamped dynamics, i.e., the peak abscissa can be assumed to coincide with the natural frequency of the associated mode. The imaging of the velocity distribution over the DEA provided by the vibrometer software allows reconstructing the mode shapes associated with each peak.

In the mechanically biased case, two vibration regimes can be identified (see Fig. 7): at low frequency, the DEA shows a pistonic motion, characterised by axial movements of the central disc (Fig. 7a), whereas at higher frequencies, the central rigid disc (whose mass is much higher that the membrane mass) does not move, and the dynamics is characterised by off-plane vibrations of the lightweight DE membrane (Fig. 7b). These higher-frequency structural vibrations have similar mode shapes at the different biasing levels, and only their natural frequency changes as a result of the initial deformation. As observed by Fox & Golbourne [11] and Garnell et al. [13] for the case of circular inflated DEAs, the structural mode shapes resemble the the known modes of a flat tensioned annular membrane with fixed edges (as graphically rendered in Fig. 7b) [40, 41], i.e., the velocity profiles are characterised by a progressively increasing

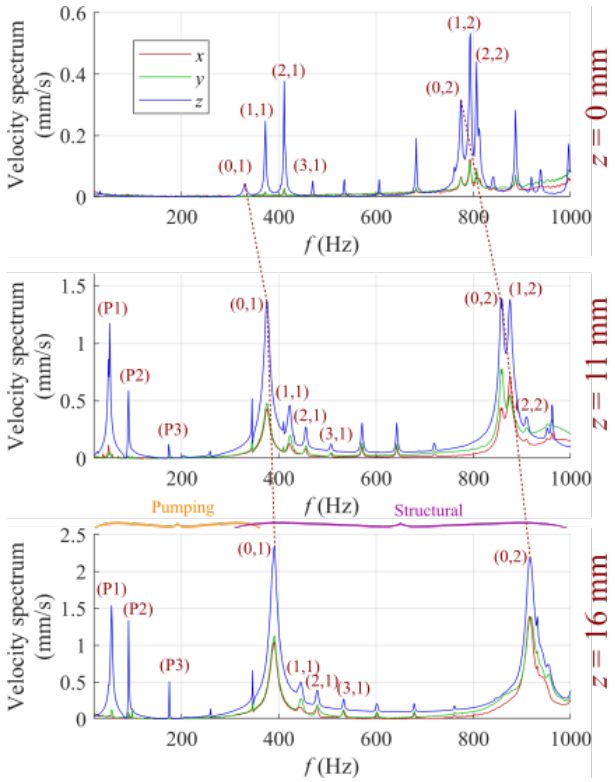

Figure 6: Average spectra of the velocity components of DEA prototype G1, subject to a bias voltage $V_b = 2000$ V and different values of the initial displacement z (namely, $z = 0,\ 11$ and 16 mm).

number of nodes in the radial and circumferential directions. We hereby refer to this modes using the standard terminology used in mechanics of vibrations: (m, n) identifies a mode shape with $m + 1$ radial nodes (including both fixed edges) and n circumferential nodes (see Fig. 7b).

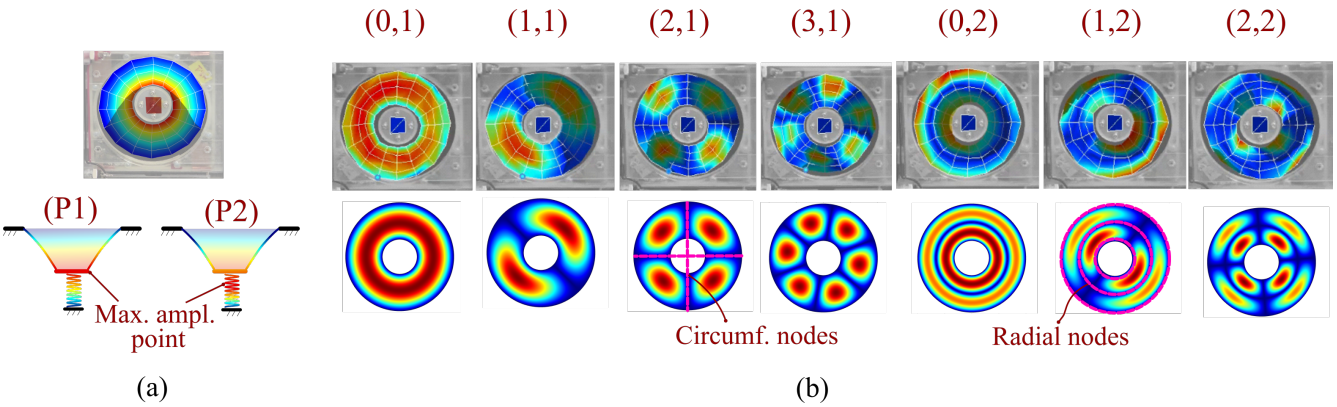

Figure 7: (a) Experimental vibrometer contour plot of the DEA velocity module in the pumping mode (top), and qualitative contour plot showing the axial velocity distribution in the DEA and the biasing spring (bottom). (b) Experimental vibrometer contour plot of the velocity module for a set of structural modes (top row), and contour plots of the corresponding modes for a flat annular membrane with fixed edges (bottom row). The labels into parentheses define the modes nomenclature.

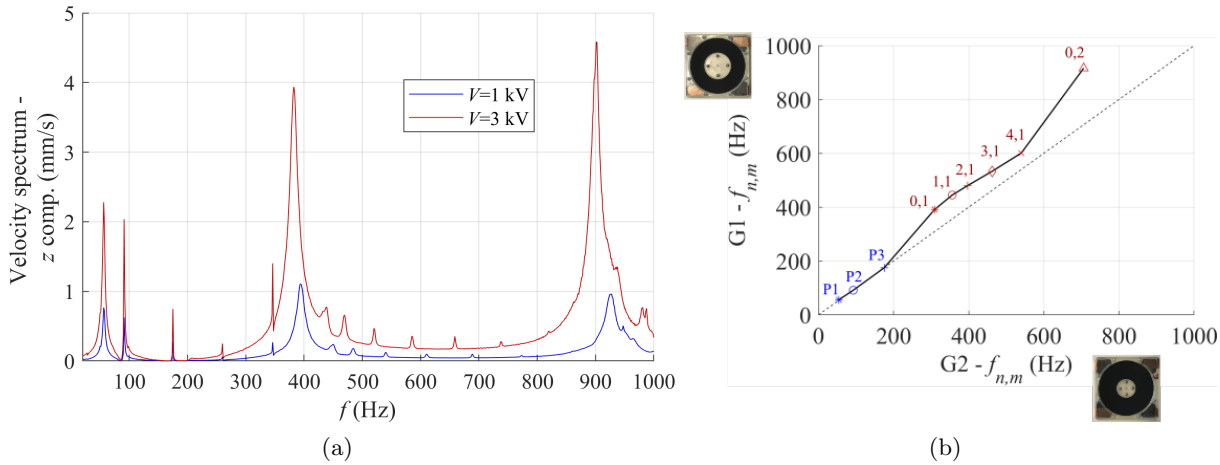

(a) (b)

Figure 8: (a) Average spectra of the z velocity components for DEA prototype G1, subject to an initial displacement $z = 16$ mm and different bias voltages ($V_b = 1$ and 3 kV). (b) Natural frequencies of a set of mode shapes for prototypes G1 and G2, subject to $V_b = 2$ kV and $z = 16$ mm. The markers represent different mode shapes, whereas the dashed line is the bisector line of the axes.

In the flat unbiased configuration, the pistonic motion that characterises the biased scenarios is not visible. As $z = 0$ is a position of mechanical singularity for the DEA, applying a voltage does not generate off-plane motions of the membrane in this position, and steady-state vibrations are only excited as a consequence of inhomogeneities in the membrane and the boundary conditions. In the biased configurations ($z \neq 0$), multiple peaks are present within the pumping region, in correspondence of all of which the DEA membrane follows a same pistonic deformation pattern. This is due to the dynamics of the biasing spring, which has a mass comparable to the total DEA mass, and behaves as a distributed oscillator, hence introducing a set of additional resonance peaks (see also Annex I). Different low-frequency peaks (P1), (P2), etc. are characterised by a same deformation pattern of the DEA membrane. The first one of these peaks corresponds to the scenario in which the stretch on the spring is uniform, whereas the others correspond to the presence of longitudinal waves on the spring (i.e., the maximum displacement point is located somewhere along the spring length).

The comparison of the plots in Fig. 6 shows that increasing the deformation z of the DEA causes an increase in the frequency of the corresponding structural modes, as a result of the increase in the stress on the membrane. Compared to the flat scenario, in which vibrations in the z direction are dominant, in the biased configurations the motion of the membrane features in-plane velocity components rendering the circumferential deformations of the membrane profile. Due to symmetry, the spectra of the x and y component are practically identical.

Although the excitation is uniform and the geometry is approximately axial-symmetrical, a set of non-axial-symmetrical mode shape peaks are present, whose steady-state oscillation is triggered by inhomogeneities and uncontrollable asymmetries in the setup. These non-symmetrical mode shapes are particularly visible at low biases, when the membrane is close to the singular configuration, and they become increasingly small (compared to the symmetrical modes $(0, m)$), or practically inexistent, as the deformation z increases. There are two axial-symmetrical structural modes ($(0, 1)$, $(0, 2)$) within the considered range, in addition to the pumping modes.

An animation of the mode shapes for the case with $z = 16$ mm (Fig. 6 - bottom) is shown in the Supplementary Material video. Notice that, unlike the axial-symmetrical modes, which show a standing-wave behaviour, some of the non-symmetrical modes (e.g. (1,1), (2,1)) exhibit travelling nodes, i.e. they be-

have as complex modes [34]. Similar to other structures, this behaviour is possibly due to aero-elastic interactions or the membrane's damping [34].

For the same DEA layout, Fig. 8a shows the influence of the biasing voltage on the velocity spectra. The plot shows that increasing the biasing voltage causes an increase in the amplitude of the oscillations. This happens because the total membrane stiffness decreases with increasing voltage (see Fig. 4b). Moreover, increasing the bias voltage results in a reduction in the natural frequencies. This happens because an increased bias voltage causes a decrease in the membrane stresses (due to the Maxwell stress component), to which the natural frequency is directly related. Such a shift in the natural frequency is much more evident in the structural modes rather than in the low-frequency pumping mode. The biasing voltages considered here correspond to relatively low electric fields of 40 and 65 kV/mm (i.e., a difference of only 25 kV/mm), hence loosely affecting the lumped axial stiffness and pumping mode frequency, but they still produce a reduction in stress which causes visible shifts at in the higher order modes frequencies.

COP-DEAs with different aspect ratios feature significantly different natural frequencies distributions. Fig. 8b shows a comparison between the two DEA geometries shown in Fig. 4a, in terms of the natural frequencies of a selection of target mode shapes. In the plot, the markers indicate different mode shapes. The natural frequencies of the low-frequency pumping modes are similar for the two DEAs, whereas significant differences emerge when the structural modes are considered. The natural frequencies are larger on membrane G1, as a result of the higher stresses to which it is subject (see Fig. 4b). In addition to that, different geometries result in different distributions of the mode shapes (i.e., the difference between the natural frequencies of consecutive modes are different).

These results suggest that, compared to the low frequency response typically exploited in DEA applications, higher-frequency structural dynamics present a greater sensitivity to the variations in the actuator geometry, pre-load, and applied electric field.

5 Model validation

Based on the experimental tests described in Sect. 4, here we present a validation of the modelling framework introduced in Sect. 3. First, attention is focused on the ability of the model in accurately predicting the natural frequencies of the COP-DEA. On this end, a three-dimensional FE analysis is employed, which allows predicting the frequencies at which different modes (including the non-axial-symmetrical ones) are excited.

The focus is then shifted on the forced dynamic response generated by the time-varying input voltage signal. In this case, only axial-symmetrical dynamics are considered, to which the largest oscillation amplitudes are associated. In fact, predicting the amplitude of the non-symmetric modes would require a deeper knowledge of the inhomogeneities in the membrane thickness, electrodes, and boundary conditions, which falls beyond the scope of this paper.

5.1 Numerical implementation

For the calculation of the structural eigenfrequencies of the DEA membranes, a FE model has been developed in Comsol multiphysics, which implements the theory described in Sect. 3.1. The FE model makes use of the Nonlinear Structural and Pressure Acoustic modules. The DE is modelled using membrane elements, that automatically implement the plane-stress condition and bending moment cancellation implicit into elastic membranes theory (see Sect. 3.1). Since the thin DE membrane can be treated as a parallel-plate capacitor, in which the electric field is simply perpendicular to the deformed electrodes

surfaces, the electrostatic problem is not solved for explicitly, and the electrostatic coupling contribution is included in the model through a simple modification of the default form of the free energy (involved in the stress computation), so as to include the voltage-dependent term present in Eq. (7)

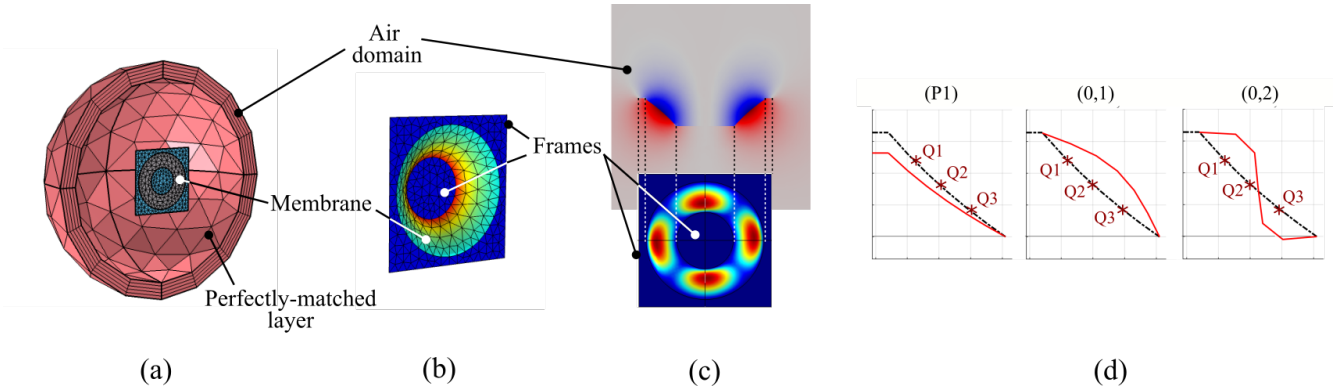

Figure 9: (a) FEM model geometry with the DEA in the flat unstretched position. (b) Deformed (pre-loaded) membrane and mesh. (c) FEM eigenfrequency analysis: contour plots of the displacement (absolute value) distribution for a reference mode (mode $(2,1)$) and corresponding contour of the air pressure distribution. (d) Profiles of the axial-symmetrical mode shapes used in the lumped-parameter model. Points Q1-Q3 are used in the analyses presented in Sect. 5.3.

For the solution of the acoustic problem, an infinitely-thin fixed 80mm×80mm square and perfectly-reflecting frame is included around the pre-stretched membrane perimeter (Fig. 9a-c). This element models, in a simplified way, the sound wave reflections from the support frame in the immediate neighbourhood of the DEA membrane. The other structural elements (support structure, spring, etc.) are not included in the modelled geometry, for simplicity. The acoustic domain is modelled as a spherical volume (with radius equal to $3.5r_o$), holding a perfectly-matched layer (with radial thickness of $0.5r_o$) on the outer surface (Fig. 9a), i.e., an artificial absorbing layer that computationally approximates an open-boundary condition [15].

The study is carried out in two steps: a stationary step in which the DEA is electro-mechanically pre-loaded to the target configuration, and a fully-coupled eigenfrequency analysis. Since in Comsol the continuum mechanics problem is formulated in a Lagrangian fashion (see Eq. (2)), whereas the acoustic problem is formulated in an Eulerian way (see Eq. (8)), the built-in moving mesh feature is employed (with the mesh displacement set equal to the membrane nodes displacements) during the static pre-load step. This allows consistent and automatic mapping of the nominal geometry into the deformed frame (Fig. 9b), and permits to use an arbitrary Lagrangian-Eulerian framework to resolve the inconsistencies among the spatial and material formulations [42, 43]. The output of the analysis are the velocity and displacement profiles for the different nodes, their natural frequencies, and the corresponding air pressure distribution profiles governing the elasto-acoustic interaction (Fig. 9c). Because of the acoustic interaction (e.g., the air radiation damping), the eigenfrequencies computed by Comsol are complex-valued. The real parts of such frequencies are then extracted, and considered as the corresponding natural frequencies of the modes.

In all the analyses, the elastic membrane response is described by means of a generalised Mooney-

Rivlin hyperelastic model in the following form:

$$\Psi_m(\mathbf{C}) = \tilde{\Psi}_m(\lambda_1, \lambda_2, \lambda_3) = \sum_{k=1}^{2} c_{k,0}(\lambda_1^2 + \lambda_2^2 + \lambda_3^2 - 3)^k + c_{0,1}(\lambda_1^{-2} + \lambda_2^{-2} + \lambda_3^{-2} - 3), \tag{20}$$

where hyperelastic parameters $c_{10} = 228.5$ kPa, $c_{20} = 8.4$ kPa, $c_{01} = -28.6$ kPa have been fitted on the tensile curves (at $V = 0$) shown in Fig. 4b, using a static version of the model presented in Sect. 3.2.1. The theoretical force-displacement curves at $V = 3$ kV in the picture have been obtained from the identified elastic parameters, using the nominal DE permittivity (Tab. 1).

The calculation of the pumping modes frequencies is performed using Eq. (22) in Annex I, and computing the DEA global axial stiffness from the reduced model in Sect. 3.2.1.

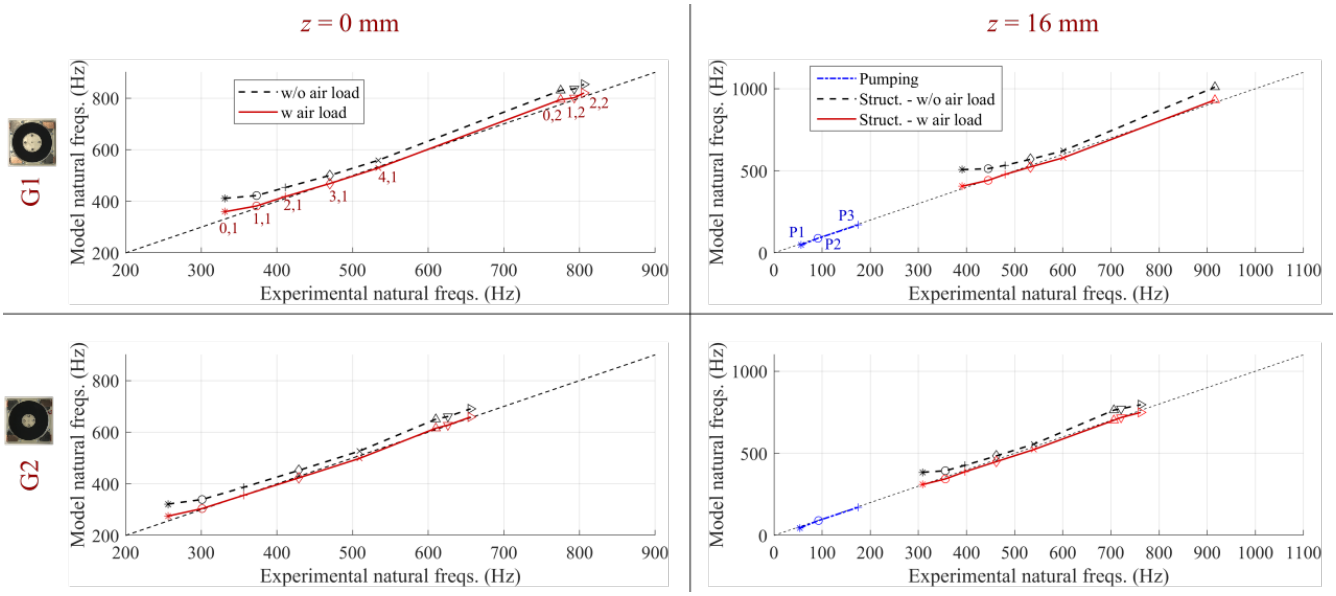

Figure 10: Comparison of experimental and model natural frequencies for a set of target modes, for two DEAs (row 1 and 2) subject to $V_b = 2$ kV. The first column refers to flat membranes with no biasing spring. The second column refers to an initial displacement $z = 16$ mm. Each marker refers to a different mode shape. Dashed-dotted lines are for low-frequency pumping modes, solid lines compare experiment and fully-coupled model (structural modes), and dashed lines compare experiments and electro-elastic model (omitting the acoustic contribution). Points lying on the dashed thin bisector line indicate a perfect agreement between model and experiments.

For the forced response, a linearised model is built using Eq. (19), calculating $\bar{\mathbf{M}}_\alpha$, $\bar{\mathbf{K}}_\alpha$ and $\bar{\mathbf{d}}_\alpha$ based on the model in Sect. 3.2.1. For the purpose of this analysis, three axial-symmetrical modes were used for the modal truncation (see Fig. 7), namely, the first pumping mode (P_1), and structural modes $(0,1)$ and $(0,2)$, whose contribution is dominant in the system response, especially in the presence of large deformations (see, e.g., bottom plot in Fig. 6). The other axial-symmetrical pumping modes, (P_2), (P_3) etc. were not included in this analysis, as their response depends on the chosen mechanical pre-loading system (here, the biasing spring) rather than the DEA itself. The analysis of their forced response hence goes beyond the aim of this paper. A discretisation of the membrane profile into $n = 6$ rings has been used for this purpose. We then compute an approximation for $\bar{\mathbf{M}}_{ad}$, based on the eigenfrequency FE analysis. Since the frequency-domain distance among the resonance peaks of the symmetrical modes is

larger than the peaks band (see, e.g., Fig. 6 - bottom), the modes are assumed uncoupled. $\bar{\mathbf{M}}_{ad}$ is thus assumed diagonal, and its elements, $m_{ad,k}$, are chosen in a way that the eigenfrequencies of the axial-symmetrical modes match the values obtained via the FE analysis (the damping is assumed low enough not to significantly affect the natural frequencies). Different values of the added mass elements $m_{ad,k}$ are calculated for each combination of mechanical pre-load z and electrical bias V_b. The added mass associated with the pumping mode is neglected ($m_{ad,1} = 0$), since it is much lower than the moving disc mass. The added mass of mode (0,1) has been found to range between 45% and 80% the structural modal mass, whereas the added mass of mode (0,2) is between 25% and 30% the modal structural mass. The added mass is higher at higher values of the off-plane deformation z, i.e., when the membrane thickness is lower and its radiating surface larger. The damping matrix $\bar{\mathbf{B}}_{\alpha}$ is also assumed diagonal, and its elements $b_{\alpha,k}$ are calibrated based on an experimental dataset (as described in detail in Sect. 5.3). In contrast with the added mass, fixed values of damping (calibrated on a specific dataset) are used for all the simulations. Since the model in Eq. (19) is linear and time-invariant, simulations are carried out in the frequency domain: the same periodic chirp excitation signal used in the tests is fed as input into the model, and the frequency-domain representation of the velocity distribution at a set of target points is obtained.

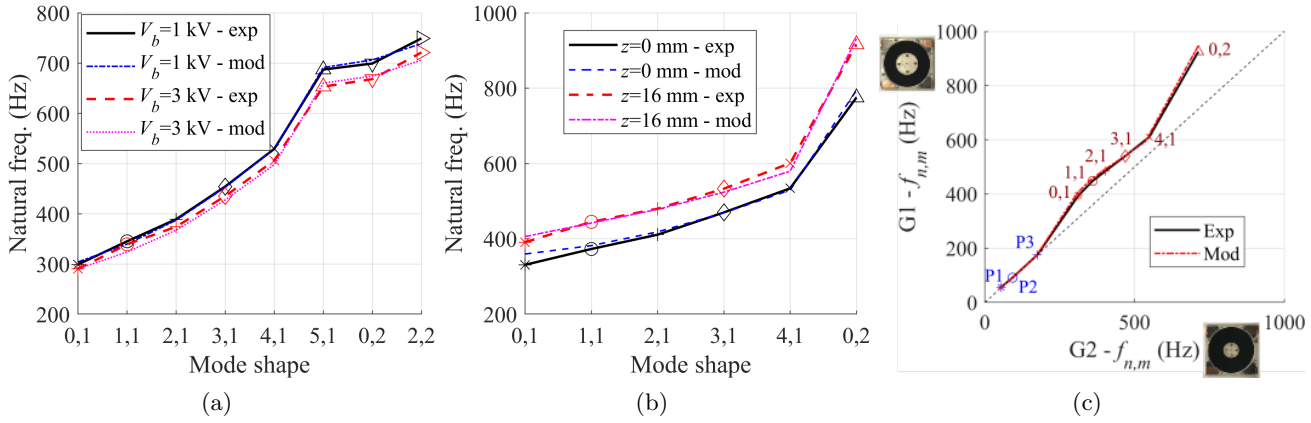

Figure 11: Prediction of how the natural frequencies are influenced by (a) the bias voltage V_b (membrane G2, $z = 12$ mm), (b) the initial deformation z (membrane G1, $V_b = 2$ kV), (c) the COP-DEA geometry ($z = 16$ mm, $V_b = 2$ kV)

5.2 Natural frequency and mode shapes analysis

A comparison of the measured and the theoretical estimated natural frequencies for a set of target modes is shown in Fig. 10 , for the two DEA geometries in Fig. 4, at two different levels of mechanical biasing (i.e., flat unbiased and out-of-plane preloaded). In the flat unbiased case structural modes are only observed, whereas in the presence of a pre-load the first three pumping frequencies are also considered. For the structural modes, experimentally observed frequencies are compared with model predictions both considering the case in which no fluid-structure interaction occurs (e.g., neglecting the contribution of the pressure), and the fully-coupled case. The plots show that the acoustic interaction has a remarkable influence on the estimated natural frequencies: the natural frequencies calculated by neglecting the air loads are up to 30% higher than those obtained from the fully-coupled model and larger than the experimental values, hence previous results relative to different DEA layouts [15]. Although some of the non-symmetrical modes are complex modes with travelling nodes (see Supplementary Material video), their shape and natural frequency is still accurately predicted by the model, owing to the low damping

to which the membrane is subject.

The fully-coupled model is able to accurately predict the natural frequencies in the different considered scenarios, with a maximum error on the order of 8%. The maximum error is on mode $(0, 1)$, which is also maximally affected by the air loading (i.e., for this mode, the difference between the natural frequency estimated with the two models versions is maximum). These discrepancies are possibly due to the simplified geometry used in the FE analysis, which neglects the presence of reflecting structural elements in the surrounding of the device. It is worth noticing that, compared with the purely structural model, the acoustically-coupled model also provides a more consistent estimate of the distribution of the natural frequencies (rendered in Fig. 12 by the curves slope), in addition to providing a better prediction of the natural frequency values.

Fig. 11 further shows that the model consistently predicts the trends of the modes' frequencies variations as a function of the design and control parameters. The structural natural frequencies decrease by increasing the voltage, due to the reduction in stress (Fig. 11a), they increase when the membrane biasing deformation is increased (Fig. 11b), and they show different values and distributions for different geometrical layouts (namely, the ratio r_o/r_i) of the COP-DEA (Fig. 11), as already observed in Sect. 4.3.

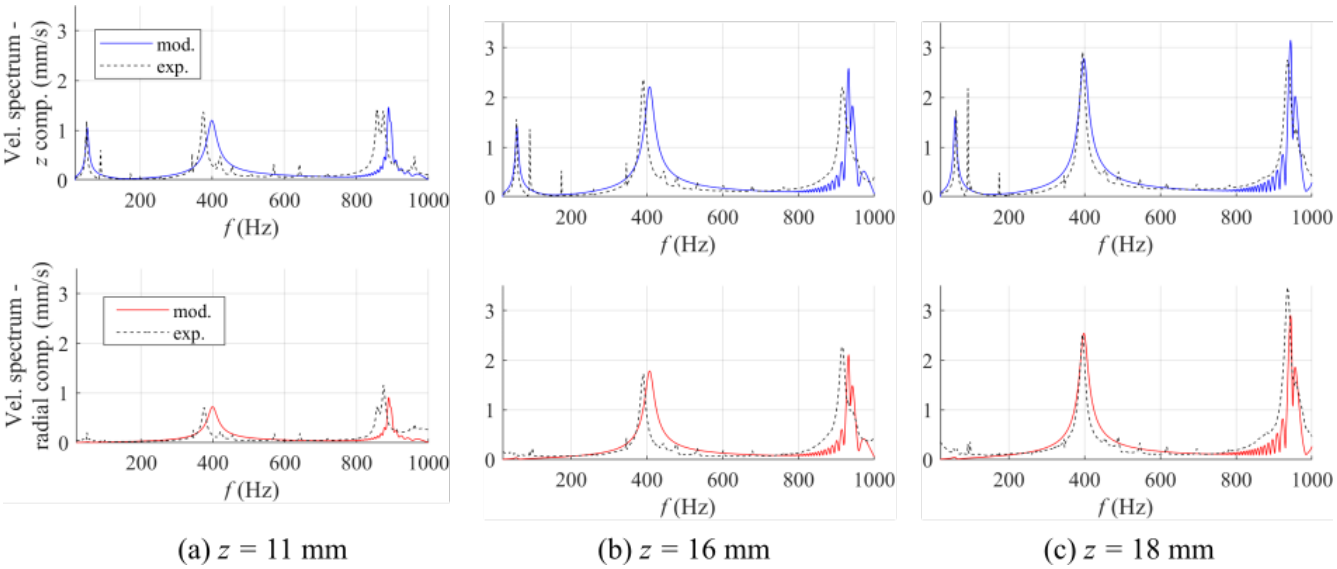

Figure 12: Comparison of model's (solid lines) and experimental (dashed lines) average spectra of the COP-DEA velocity components at three different initial deformations: (a) $z = 11$ mm, (b) $z = 16$ mm, (c) $z = 18$ mm - membrane G1, $V_b = 2$ kV.

5.3 Forced response analysis

Validation of the reduced axial-symmetrical model of the forced dynamic response of the COP-DEA is carried out by comparing the measured velocity spectra and those predicted by the reduced model in Sect. 3.2 (Eq. (19)).

Comparisons are focused both on the average spectra and on local spectra of the individual points. Since the considered model is axial-symmetrical, two velocity components are considered, namely the axial and the radial velocity (as opposed to the cartesian components provided by the vibrometer), where the average experimental radial velocity spectra are calculated from the vibrometer's spectra of the cartesian components.

With reference to membrane G1, Fig. 12 shows a comparison between the experimental and model-predicted velocity spectra for different values of the mechanical biasing z.

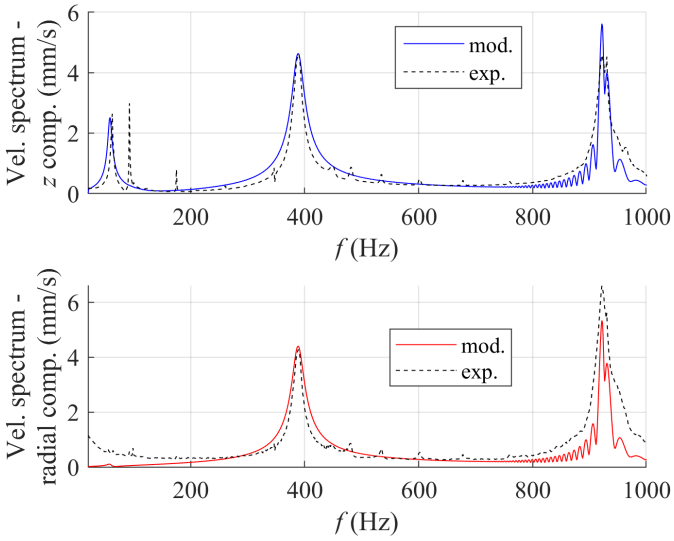

Figure 13: Comparison of model's (solid lines) and experimental (dashed lines) average spectra of the COP-DEA velocity components for membrane G1 at $V_b = 3$ kV
and $z = 18$ mm.

The dataset in Fig. 12b (relative to an intermediate bias of $z = 16$ mm) has been used for the calibration of the damping coefficients. Since the frequency passbands of the different modes practically do not overlap, the damping coefficients for the different modes were calculated independently from each other. Each element of the diagonal damping matrix $\bar{\mathbf{B}}_\alpha$ (see Eq. (19)) has been chosen in such a way that the height (average of axial and radial component) of the associated peak equals that of the experimental spectra. The identified values of the modal damping coefficients (divided by the modal structural masses) are: $b_{\alpha,1}/m_{\alpha,1} = 45$ s^{-1} for mode (P1), $b_{\alpha,2}/m_{\alpha,2} = 245$ s^{-1} for mode (0,1) and $b_{\alpha,3}/m_{\alpha,3} = 57$ s^{-1} for (0,2). These same values of the damping-to-structural-mass ratio have been then used for the comparisons drawn in Fig. 12a and c, as well as the other comparisons presented in the following. These correspond, in all cases, to damping ratios below 10^{-3}.
Based on Fig. 12, the model shows a good agreement with the experimental data, as it is able, with a relatively modest calibration, to predict the trends in the velocity amplitudes at different values if z. In particular, the model captures the amplitudes of both velocity components, hence consistently predicting the amount of radial displacement generated by the off-plane deformations. The mismatches between models and experiments are basically due to errors in the estimate of the modes' natural frequencies by the model, which, although rather small in percentage (as discussed in Sect. 5.2), result is a misalignment between the model and experimental peaks.

The calibrated model is then used to evaluate the modifications in the spectrum obtained by changing the bias voltage V_b. With reference to the same DEA geometry and initial deformation considered in Fig. 12c, Fig. 13 compares the spectra obtained using a larger value of the biasing voltage. Although a same excitation amplitude $\tilde{V}$ is used in both tests, the reduction in stiffness due to the Maxwell stress generates increases on the order of 30-40% in the amplitude of the different resonance peaks, which are consistently captured by the model.

In addition to the presented average spectra comparisons, Fig. 14 shows a comparison in terms of

the velocity spectra at different target points on the membrane, so as to prove that the model succeeds in describing the local behaviour of the DEA. Reference is made to points Q1, Q2 and Q3 (as defined in Fig. 5d), which roughly lie at a distance of 1/4, 1/2, and 3/4 the membrane radial width $(r_o - r_i)$ from the electrode inner circumference.

Compared to the average spectrum (at the same voltage and deformation) shown in Fig. 12, the point spectra individually show higher/lower amplitude of the different peaks, based on the relative position of the considered points and mode shapes (see Fig. 9d). In particular, point Q2 lies in proximity of a crest point for mode $(0, 1)$, and hence shows larger amplitude at the second peak compared to the other points. The same point lies in proximity of a node point for mode $(0, 2)$, hence exhibiting a relatively small amplitude of the third peak. In contrast, points Q1 and Q3 are close to a crest point for mode $(0, 2)$, and feature maximum velocity amplitude at the natural frequency of that mode. Though calibrated on the average spectrum response (Fig. 12b), the model fully describes the above mentioned trends, and it is thus able to predict how the velocity profiles change throughout the membrane and assess how much the different mode shapes weight on the response of different points.

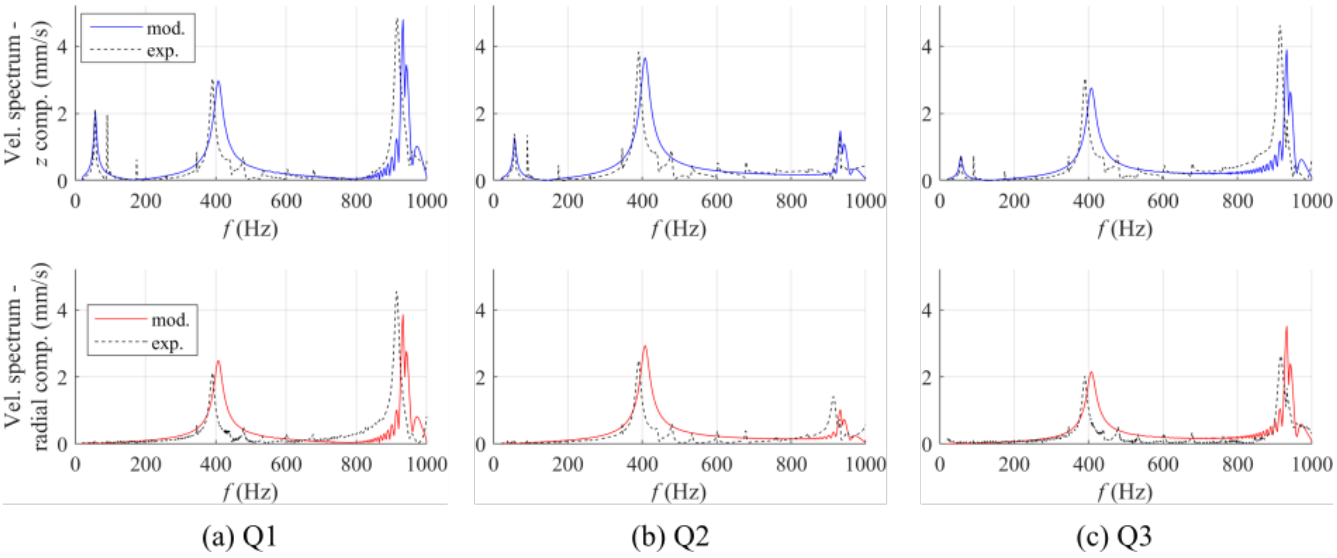

Figure 14: Comparison of model's (solid lines) and experimental (dashed lines) spectra of the COP-DEA velocity components of three different points (Q1, Q2, Q3) on the DEA membrane - membrane G1, $V_b = 2$ kV, $z = 16$ mm.

In conclusion, the presented lumped parameter model of the COP-DEA forced excitation makes use of a low number of experimentally-calibrated parameters (a value of damping for each modal shape, identified based on the system average response), and it is able to predict the trends of the DEA membrane velocity components variations as a function of the bias voltage and deformation, and what the spatial distribution of the velocities components is.

6 Conclusions

We presented a mathematical model and experimental characterisation of voltage-driven structural vibrations in dielectric elastomer actuators (DEAs).

Although most DEA topologies normally exploit a dominant predefined deformation mode (namely, a pumping mode), the polymeric dielectric membranes are elastic continua that, subject to high frequency

alternated current or broadbanded electrical excitation, exhibit a complex set of structural mode shapes and deformation patterns. Taking advantage of such higher order modes potentially allows using DEAs for a completely new set of applications, such as morphing conformable structures, tunable optical or acoustic systems.

In this work, reference is made on a widely investigated DEA layout, called a circular out-of-plane DEA (COP-DEA). This device does not require any pressure biasing or sealed air volumes, as it makes use of elastic springs to provide an initially flat DEA membrane with the off-plane pre-load required for actuation.

We performed tests on different silicone-based COP-DEA geometries subject to different mechanical pre-loads and voltage biasing. Using a scanning laser Doppler vibrometer, we could measure the velocity spectra generated by multi-chromatic voltage inputs at different points over the DEA surface, and the mode shapes that are excited at the different frequencies.

At low excitation frequency, the membrane shows a pistonic axial motion, whereas at higher frequency a complex set of mode shapes appear. Because of the large mass of the structural components (moving rigid fixtures, biasing spring), the pistonic motion completely disappears in the frequency range where higher order structural modes are excited. At low frequencies, the biasing spring element introduces a set of resonance peaks in the DEA response, due to its own structural dynamics. Choosing a suitable combination of the biasing element stiffness and mass is therefore crucial, if COP-DEA with a flat frequency-response are sought. In spite of the circular geometry of the DEA and the uniform excitation, complex circumferential modes are detected on the membrane at high frequency, at least in the neighbourhood of the flat singular configuration. As expected, by increasing the off-plane deformation, the influence of such circumferential modes becomes increasingly small compared to the dominant axial-symmetrical modes.

We were able to explain the observed mode shapes and their natural frequency using a fully-coupled finite-element model. The model relies on the assumption the the active material can be treated as a thin hyperleastic membrane with dielectric properties, and is thus potentially suitable to describe COP-DEAs made of a wide variety of dielectric elastomer materials. Similar to previous works on different DEA topologies, we observed that the air pressure loads (generated by the DEA vibrations) significantly affect the natural modes' frequency, as they provide the system with a non-negligible aerodynamic added mass. Using information from the FE formulation, we built a lumped-parameter model that, by relying on a modal decomposition, describes the forced dynamic response of the COP-DEA, and is able to predict the profiles of the different velocity components at different points within the considered frequency range.
The developed modelling framework might be used, in the future, for the design of multi-function actuators that exploit different vibration regimes (pumping and structural modes) over different frequency ranges, and the definition of control strategies aimed at the selective excitation of target vibration modes.

Acknowledgements

This project has received funding from the European Union's Horizon 2020 research and innovation programme under the Marie Skłodowska-Curie grant agreement No 893674 (DEtune).

References

[1] E. Hajiesmaili and D. R. Clarke, "Dielectric elastomer actuators," *Journal of Applied Physics*, vol. 129, no. 15, p. 151102, 2021.

[2] Y. Chen, L. Agostini, G. Moretti, M. Fontana, and R. Vertechy, "Dielectric elastomer materials for large-strain actuation and energy harvesting: a comparison between styrenic rubber, natural rubber and acrylic elastomer," *Smart Materials and Structures*, vol. 28, no. 11, p. 114001, 2019.

[3] R. Heydt, R. Pelrine, J. Joseph, J. Eckerle, and R. Kornbluh, "Acoustical performance of an electrostrictive polymer film loudspeaker," *The Journal of the Acoustical Society of America*, vol. 107, no. 2, pp. 833–839, 2000.

[4] N. Hosoya, H. Masuda, and S. Maeda, "Balloon dielectric elastomer actuator speaker," *Applied Acoustics*, vol. 148, pp. 238–245, 2019.

[5] G.-Y. Gu, J. Zhu, L.-M. Zhu, and X. Zhu, "A survey on dielectric elastomer actuators for soft robots," *Bioinspiration & biomimetics*, vol. 12, no. 1, p. 011003, 2017.

[6] C. Cao, X. Gao, and A. T. Conn, "A magnetically coupled dielectric elastomer pump for soft robotics," *Advanced Materials Technologies*, vol. 4, no. 8, p. 1900128, 2019.

[7] H. Zhao, A. M. Hussain, A. Israr, D. M. Vogt, M. Duduta, D. R. Clarke, and R. J. Wood, "A wearable soft haptic communicator based on dielectric elastomer actuators," *Soft robotics*, vol. 7, no. 4, pp. 451–461, 2020.

[8] F. Carpi, G. Frediani, S. Turco, and D. De Rossi, "Bioinspired tunable lens with muscle-like electroactive elastomers," *Advanced functional materials*, vol. 21, no. 21, pp. 4152–4158, 2011.

[9] T. Hiruta, N. Hosoya, S. Maeda, and I. Kajiwara, "Experimental validation of vibration control in membrane structures using dielectric elastomer actuators in a vacuum environment," *International Journal of Mechanical Sciences*, vol. 191, p. 106049, 2021.

[10] G. Moretti, S. Rosset, R. Vertechy, I. Anderson, and M. Fontana, "A review of dielectric elastomer generator systems," *Advanced Intelligent Systems*, vol. 2, no. 10, p. 2000125, 2020.

[11] J. Fox and N. Goulbourne, "On the dynamic electromechanical loading of dielectric elastomer membranes," *Journal of the Mechanics and Physics of Solids*, vol. 56, no. 8, pp. 2669–2686, 2008.

[12] J. Fox and N. Goulbourne, "Electric field-induced surface transformations and experimental dynamic characteristics of dielectric elastomer membranes," *Journal of the Mechanics and Physics of Solids*, vol. 57, no. 8, pp. 1417–1435, 2009.

[13] E. Garnell, C. Rouby, and O. Doaré, "Dynamics and sound radiation of a dielectric elastomer membrane," *Journal of Sound and Vibration*, vol. 459, p. 114836, 2019.

[14] C. H. Jenkins and U. A. Korde, "Membrane vibration experiments: An historical review and recent results," *Journal of Sound and Vibration*, vol. 295, no. 3-5, pp. 602–613, 2006.

[15] E. Garnell, O. Doaré, and C. Rouby, "Coupled vibro-acoustic modeling of a dielectric elastomer loudspeaker," *The Journal of the Acoustical Society of America*, vol. 147, no. 3, pp. 1812–1821, 2020.

[16] M. Gareis and J. Maas, "Modal analysis of circular buckling dielectric elastomer transducers," in *Electroactive Polymer Actuators and Devices (EAPAD) XXIII*, vol. 11587, p. 1158722, International Society for Optics and Photonics, 2021.

[17] S. Nalbach, G. Rizzello, and S. Seelecke, "Experimental analysis of continuous vibrations in dielectric elastomer membrane actuators via three-dimensional laser vibrometry," *Journal of Vibration and Acoustics*, vol. 141, no. 5, 2019.

[18] G. Berselli, R. Vertechy, G. Vassura, and V. Parenti-Castelli, "Optimal synthesis of conically shaped dielectric elastomer linear actuators: design methodology and experimental validation," *IEEE/ASME Transactions on Mechatronics*, vol. 16, no. 1, pp. 67–79, 2011.

[19] C. Cao, X. Gao, S. Burgess, and A. T. Conn, "Power optimization of a conical dielectric elastomer actuator for resonant robotic systems," *Extreme Mechanics Letters*, vol. 35, p. 100619, 2020.

[20] P. Linnebach, G. Rizzello, and S. Seelecke, "Design and validation of a dielectric elastomer membrane actuator driven pneumatic pump," *Smart Materials and Structures*, 2020.

[21] T. Sugimoto, A. Ando, K. Ono, Y. Morita, K. Hosoda, D. Ishii, and K. Nakamura, "A lightweight push-pull acoustic transducer composed of a pair of dielectric elastomer films," *The Journal of the Acoustical Society of America*, vol. 134, no. 5, pp. EL432–EL437, 2013.

[22] T. He, L. Cui, C. Chen, and Z. Suo, "Nonlinear deformation analysis of a dielectric elastomer membrane–spring system," *Smart Materials and Structures*, vol. 19, no. 8, p. 085017, 2010.

[23] G. Rizzello, M. Hodgins, D. Naso, A. York, and S. Seelecke, "Modeling of the effects of the electrical dynamics on the electromechanical response of a DEAP circular actuator with a mass–spring load," *Smart Materials and Structures*, vol. 24, no. 9, p. 094003, 2015.

[24] G. Moretti, G. Rizzello, M. Fontana, and S. Seelecke, "A multi-domain dynamical model for cone-shaped dielectric elastomer loudspeakers," in *Electroactive Polymer Actuators and Devices (EAPAD) XXIII*, vol. 11587, p. 115871K, International Society for Optics and Photonics, 2021.

[25] G. A. Holzapfel, *Nonlinear solid mechanics - A continuun approach for Engineering*, vol. 24. Wiley Chichester, 2000.

[26] R. van Kessel, P. Bauer, and J. A. Ferreira, "Electrical modeling of cylindrical dielectric elastomer transducers," *Smart Materials and Structures*, vol. 30, no. 3, p. 035021, 2021.

[27] P. Wriggers, "Basic equations of continuum mechanics," in *Nonlinear Finite Element Methods*, pp. 19–102, Springer, 2008.

[28] P. Steinmann, M. Hossain, and G. Possart, "Hyperelastic models for rubber-like materials: consistent tangent operators and suitability for treloar's data," *Archive of Applied Mechanics*, vol. 82, no. 9, pp. 1183–1217, 2012.

[29] G. Rizzello, P. Loew, L. Agostini, M. Fontana, and S. Seelecke, "A lumped parameter model for strip-shaped dielectric elastomer membrane transducers with arbitrary aspect ratio," *Smart Materials and Structures*, vol. 29, no. 11, p. 115030, 2020.

[30] L. E. Kinsler, A. R. Frey, A. B. Coppens, and J. V. Sanders, *Fundamentals of acoustics*. John Wiley and Sons, 1999.

[31] F. Ma and C. Ng, "On the orthogonality of natural modes of vibration," *Mechanics Research Communications*, vol. 31, no. 3, pp. 295–299, 2004.

[32] L. Meirovitch, *Analytical methods in vibrations.* The Macmillan Company, New York, 1967.

[33] M. Aenlle, M. Juul, and R. Brincker, "Modal mass and length of mode shapes in structural dynamics," *Shock and Vibration*, vol. 2020, 2020.

[34] S. Adhikari, "Optimal complex modes and an index of damping non-proportionality," *Mechanical systems and signal processing*, vol. 18, no. 1, pp. 1–27, 2004.

[35] B. Fasolt, M. Hodgins, G. Rizzello, and S. Seelecke, "Effect of screen printing parameters on sensor and actuator performance of dielectric elastomer (de) membranes," *Sensors and Actuators A: Physical*, vol. 265, pp. 10–19, 2017.

[36] "Elastosil 2030 films catalogue, Wacker." https://www.wacker.com/h/medias/7091-EN.pdf.

[37] M. Hodgins, G. Rizzello, A. York, D. Naso, and S. Seelecke, "A smart experimental technique for the optimization of dielectric elastomer actuator (dea) systems," *Smart Materials and Structures*, vol. 24, no. 9, p. 094002, 2015.

[38] G. Moretti, L. Sarina, L. Agostini, R. Vertechy, G. Berselli, and M. Fontana, "Styrenic-rubber dielectric elastomer actuator with inherent stiffness compensation," in *Actuators*, vol. 9, p. 44, Multidisciplinary Digital Publishing Institute, 2020.

[39] Polytec GmbH, *Polytec scanning vibrometer - theory manual*, 2010.

[40] G. R. Sharp, "Finite transform solution of the symmetrically vibrating annular membrane," *Journal of Sound and Vibration*, vol. 5, no. 1, pp. 1–8, 1967.

[41] M. Jabareen and M. Eisenberger, "Free vibrations of non-homogeneous circular and annular membranes," *Journal of Sound and Vibration*, vol. 240, no. 3, pp. 409–429, 2001.

[42] Comsol, *COMSOL Multiphysics - Reference manual*, 5.5 ed., 2019.

[43] N. B. Roozen, T. Rutjes, and H. Nijmeijer, "Vibro-acoustic radiation of rigid bodies oscillating at large amplitude and low mach number: Modelling and experiments," *Journal of sound and vibration*, vol. 329, no. 26, pp. 5532–5545, 2010.

ANNEX I: Effect of the biasing element mass on the COP-DEA low-frequency response

If the mass M_s of the biasing spring is comparable with the mass of the central disc, the continuum dynamics of the spring affects the dynamics of the system, introducing additional modes. Since both the mass of the spring and the central disc are much larger than the DE mass, these effects are only relevant in the low frequency range. In this range, the DEA moves pistonically, and the coupled DEA-spring system can be modelled as in Fig. 15 , where k_{DE} is an equivalent pumping-mode DEA stiffness (calculated from the slope of the DEA force-displacement response in the neighbourhood of the equilibrium state, at a given bias voltage), and the spring mass M_s is uniformly distributed over the spring length.

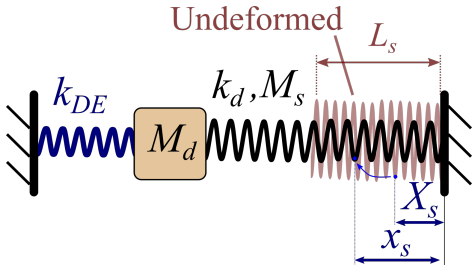

Figure 15: Low-frequency mechanical equivalent model of the DEA-spring system

We denote X_s the position of a material point of the spring in the undeformed configuration, and $x_s(X_s, t)$ the time-varying position of the same point in a deformed state. The dynamics of the system is described by the following partial differential equation and boundary conditions:

$$\begin{cases} \dfrac{\partial^2 x_t}{\partial t^2} = c_s^2 \dfrac{\partial^2 x_t}{\partial X_s^2} \\ x_s(0,t) = 0 \\ M_d c_s^2 \left.\dfrac{\partial x_t}{\partial t^2}\right|_{L_s} + k_d L_s \left.\dfrac{\partial x_t}{\partial X_s}\right|_{L_s} + k_{DE} x_t(L_s, t) = 0 \end{cases} \tag{21}$$

where the first equation describes the dynamics of longitudinal waves on a spring, whose speed is $c_s = (k_d L_s^2/M_s)^{0.5}$. The second boundary condition in Eq. (21), at $X_s = L_s$ is the linearised equation of motion of the DEA lumped mass M_d.
The corresponding eigenvalue problem associated with the partial differential equation is as follows:

$$-M_d \omega_{k,s}^2 \sin\left(\frac{\omega_{k,s}}{c_s} L_s\right) + k_d L_s \frac{\omega_{k,s}}{c_s} \cos\left(\frac{\omega_{k,s}}{c_s} L_s\right) + k_{DE} \sin\left(\frac{\omega_{k,s}}{c_s} L_s\right) = 0, \tag{22}$$

and it provides a set of additional natural frequencies $\omega_{k,s}$ for the system generated by the structural dynamics of the biasing spring. The corresponding eigenvector shape-function $\tilde{x}_{t,k}$, rendering pumping mode shape (P_k), is:

$$\tilde{x}_{t,k}(X_s) = \sin\left(\frac{\omega_{k,s}}{c_s} X_s\right). \tag{23}$$

Here, $\omega_{k,s}$ and $\tilde{x}_{t,k}$ are respectively the natural frequency and the mode shape of mode (P_k).